

1 **Cardiolipin dynamics promote membrane remodeling by mitochondrial**
2 **OPA1**

3
4
5 Sirikrishna Thatavarthy^{a,†}, Luciano A. Abriata^{b,c,d,†}, Fernando Teixeira Pinto Meireles^{b,d}, Kelly E.
6 Zuccaro^e, Akhil Gargy Iragavarapu^a, Gabriela May Sullivan^e, Frank R. Moss III^f, Adam Frost^f,
7 Matteo Dal Peraro^{b,d,*}, and Halil Aydin^{a,e,g,*}

8
9
10 ^aDepartment of Molecular Pathobiology, College of Dentistry, New York University, New York,
11 NY, USA; ^bInstitute of Bioengineering, School of Life Sciences, École Polytechnique Fédérale de
12 Lausanne, CH-1015 Lausanne, Switzerland; ^cProtein Production and Structure Core Facility,
13 School of Life Sciences, École Polytechnique Fédérale de Lausanne, CH-1015 Lausanne,
14 Switzerland; ^dSwiss Institute of Bioinformatics, CH-1015 Lausanne, Switzerland; ^eDepartment of
15 Biochemistry, University of Colorado Boulder, Boulder, Colorado, USA; ^fAltos Labs, Bay Area
16 Institute of Science, San Francisco, CA, USA; ^gNYU Pain Research Center, New York University,
17 New York, NY, USA.

18
19
20 [†]These authors contributed equally to this work.

21
22
23 *Corresponding author. Email: matteo.dalperaro@epfl.ch; halil.aydin@nyu.edu

25 **Abstract**

26 Cardiolipin (CL) is a mitochondria-specific phospholipid that forms heterotypic interactions with
27 membrane-shaping proteins and regulates the dynamic remodeling and function of mitochondria.
28 However, the precise mechanisms through which CL influences mitochondrial morphology are
29 not well understood. In this study, employing molecular dynamics (MD) simulations, we
30 determined that CL molecules extensively engage with the paddle domain (PD) of mitochondrial
31 fusion protein Optic Atrophy 1 (OPA1), which controls membrane-shaping mechanisms.
32 Structure-function analysis confirmed the interactions between CL and two conserved motifs of
33 OPA1 at the membrane-binding sites. We further developed a bromine-labeled CL probe to
34 enhance cryoEM contrast and characterized the structure of OPA1 assemblies bound to the CL-
35 brominated lipid bilayers. Our images provide direct evidence of CL enrichment within the OPA1-
36 binding leaflet. Last, we observed a decrease in membrane remodeling activity for OPA1 in lipid
37 compositions with increasing concentrations of monolysophosphatidylcholine (MLCL). This suggests that
38 the partial replacement of CL by MLCL, as observed in Barth syndrome-associated mutations of
39 the tafazzin phospholipid transacylase, alters the malleability of the membrane and compromises
40 proper remodeling. Together, these data provide insights into how biological membranes regulate
41 the mechanisms governing mitochondrial homeostasis.

42

43 **Introduction**

44 The proper spatial and temporal organization of organelles underlies many cellular processes,
45 ranging from division and differentiation to apoptosis and communication¹. Within a cell,
46 mitochondria are mainly organized into highly dynamic and interconnected networks, whose
47 diverse functions are dependent on their complex structure and organization². Mitochondria are
48 double-membrane bound organelles that consist of four major compartments: the outer
49 membrane (OM), intermembrane space (IMS), inner membrane (IM), and matrix³. The
50 mitochondrial IM folds inwards to form the organelle's hallmark cristae membranes, which harbor
51 the respiratory supercomplexes that produce ATP via oxidative phosphorylation (OXPHOS)⁴. In
52 addition to their role in energy production, mitochondria are involved in the metabolism of amino
53 acids, lipids, and nucleotides, transport of metabolites and ions, reactive oxygen species (ROS)
54 production, and signaling^{4,5}. The molecular regulation of mitochondrial architecture, which is
55 controlled by the membrane-shaping lipids and proteins, is critical for tuning the activity of these
56 key processes and preserving homeostasis^{6–11}. Hence, mitochondrial function is intimately linked
57 to dynamic changes in mitochondrial morphology and can influence human health and disease¹².

58

59 The main lipid components of mitochondrial membranes are phospholipids^{13,14}. Cardiolipin (CL)
60 is a mitochondrion-specific phospholipid primarily located in the mitochondrial inner membrane
61 (IM), where it accounts for ~20% of the lipid content^{13,14}. Characterized by a unique chemical
62 structure consisting of a double glycerophosphate backbone and four fatty acyl chains¹⁵, CL
63 undergoes maturation through biosynthesis and remodeling processes catalyzed by different
64 enzymes within mitochondria^{16–19}. Mature CL molecules interact with and regulate several pivotal
65 proteins in mitochondria, including those involved in the regulation of mitochondrial morphology^{20–}
66 ²⁶. Aberrant CL content, structure, and localization result in mitochondrial defects and cellular
67 dysfunction, leading to the development of cardiovascular diseases²⁷, impaired neuronal function
68 ²⁸, and neurodegeneration^{29,30}. Barth syndrome, an X-linked disease conventionally characterized
69 by dilated cardiomyopathy, skeletal myopathy, cyclic neutropenia, arrhythmias, growth
70 retardation, and cognitive dysfunction, occurs in 1 in 300,000 to 400,000 births^{31–33}. The
71 predominant locus for this disorder has been mapped to the distal region of chromosome Xq28,
72 which encodes the human tafazzin (TAZ)^{32,34}. TAZ functions as a phospholipid transacylase,
73 facilitating the transfer of acyl groups from phospholipids to monolysocardiolipin (MLCL) to
74 generate mature CL species^{16,35}. Mutations associated with Barth syndrome compromise TAZ
75 function, resulting in alterations in CL level and molecular composition, along with defects in
76 mitochondrial architecture and function^{36–39}. Despite extensive research on the pathophysiology

77 of abnormal CL acyl composition arising from defective remodeling in cellular models, the
78 molecular mechanisms connecting MLCL accumulation and protein function remain poorly
79 understood.

80
81 CL plays an essential role in regulating the shape and stability of the mitochondrial IM by forming
82 critical interactions with mitochondria-shaping proteins, determining the spatial identity and fitness
83 of the organelle^{21,40,41}. One such key protein involved in the modulation of mitochondrial
84 architecture is optic atrophy 1 (OPA1), a mechano-chemical enzyme that catalyzes the fusion of
85 mitochondrial IM, reorganizes dynamic cristae structure, and influences OXPHOS efficiency,
86 apoptosis, reactive oxygen species production, and mtDNA maintenance^{42–46}. In humans, the
87 OPA1 precursor gives rise to eight isoforms, all of which are directed to the mitochondrial
88 intermembrane space (IMS)⁴⁷. Subsequently, divergent proteolytic mechanisms first cleave the
89 mitochondrial-targeting sequence (MTS) to produce the long form (L-OPA1), which is N-terminally
90 anchored to the inner membrane (IM), followed by the generation of the short form (S-OPA1)
91 devoid of the transmembrane (TM) domain^{48,49}. Both L-OPA1 and S-OPA1 assemble into
92 oligomers and participate in membrane remodeling, and are essential for maintaining
93 mitochondrial organization⁴⁹. All OPA1 variants and proteoforms assemble into higher-order
94 oligomers in the presence of CL-containing membranes^{10,11,50–52}. This CL-OPA1 interaction is
95 sufficient to activate membrane fusion and uphold cristae structural integrity, thus highlighting the
96 regulatory role of CL in mitochondrial remodeling and function.

97
98 Understanding the precise molecular interactions between key mitochondrial proteins and CL
99 within intact membranes has not been possible because single-phase fluid bilayers are generally
100 thought to lack a structured pattern at the nanoscale. Hence, our understanding of molecular
101 mechanisms connecting CL and mitochondrial protein function remains incomplete. To address
102 this challenge and investigate CL's functional role within the structural organization of
103 mitochondrial membranes, we conducted molecular dynamics (MD) simulations, performed
104 biochemical studies, and devised a novel lipid labeling approach for CL localization in electron
105 cryo-microscopy (cryoEM) maps. Our findings reveal how CL regulates the activity of
106 mitochondria-shaping human OPA1 to maintain mitochondrial homeostasis and provide a
107 molecular explanation for the mechanisms underlying the disruptive effects of MLCL accumulation
108 on mitochondrial membrane dynamics.

109

110 **Results**

111 **Microsecond CG MD simulations reveal OPA1 membrane binding sites**

112 In a recent study, we reported the cryoEM structures of human S-OPA1 helical assemblies bound
113 to CL-containing lipid tubes¹⁰. These findings unveiled the architecture of assembled OPA1 and
114 large structural arrangements potentially involved in catalyzing mitochondrial IM fusion. However,
115 the mechanistic understanding of how OPA1 molecules selectively engage with CL-enriched
116 membranes to modulate mitochondrial morphology remains unclear. To understand the molecular
117 basis of CL-dependent mitochondrial remodeling, we conducted coarse-grained molecular
118 dynamics (CG MD) simulations on microsecond time scales using S-OPA1 tetramers and lipid
119 bilayers mimicking the composition of the mitochondrial IM^{13,14}. While human S-OPA1 forms
120 micron-scale helical filaments upon membrane binding¹⁰, simulating filamentous assemblies over
121 relevant timescales proved not feasible due to their large size. Instead, we focused on tetrameric
122 arrangements of S-OPA1 proteins, which encompass all key assembly interfaces and are
123 tractable through multi-microsecond sampling at the coarse-grained level. To initiate simulations,
124 we extracted four different tetrameric subassemblies (tetramers 1 to 4) of S-OPA1 models
125 representing various oligomeric and functional states of the protein from the cryoEM helical
126 reconstruction of the membrane-bound human S-OPA1 polymer (Figs. 1a-b and Supplementary
127 Fig. S1). These assemblies were manually positioned with their membrane-interacting surface
128 proximal to, but not fully inserted into, a model membrane composed of a mixture of MARTINI
129 lipids POPC, POPE, and CL(18:1)₄ at a ratio of ~4:4:2, respectively (Supplementary Figs. S2a-
130 c). The protein-membrane systems were parameterized with MARTINI22P, reaching close to 1
131 million beads that represent ~10 million atoms in each system. We simulated each of these 4
132 tetrameric systems for over 8 μ s to assess whether and how the tetramers engage with the
133 membranes. Tetramer 1, representative of the conserved crisscross association of dynamin
134 superfamily proteins⁵³, was simulated in three independent replicas to maximize sampling and
135 allow for the most accurate comparisons (Fig. 1c).

136

137 Upon visual inspection, all four subunits of tetramer 1 exhibit clear and strong membrane binding
138 within the first few hundred nanoseconds. In this timescale, the highly conserved membrane-
139 inserting loop (MIL) region (⁷⁷¹WKKRWLYWKNR⁷⁸¹) of the paddle domain (PD) inserts into the
140 lipid bilayer, firmly anchoring the assembly tightly onto the membrane (Fig. 1c, and
141 Supplementary Figs. S2a-c and S5). A second highly conserved site within the PD (⁸⁵⁷RRGFY⁸⁶¹),
142 which we refer to hereafter as the “docking region”, also interacts with membranes, albeit
143 peripherally. The docking region does not embed in the membrane but remains stably bound

144 throughout the simulation, as quantified below through lipid-protein contact residence times
145 (Supplementary Figs. S2a-c and S5). To address potential biases that may arise due to the initial
146 proximity of S-OPA1 tetramers to the membrane (~6 Å), we conducted a supplementary set of
147 CG MD simulations. In this series, a single subunit of S-OPA1 tetramer 1 was initially positioned
148 60 Å away from the model membrane (Supplementary Fig. S2b). Across all five replicas, the S-
149 OPA1 monomer eventually encountered the membrane. In four of the replicas, extended
150 interactions between S-OPA1 and the bilayer were observed.

151

152 **CL molecules cluster at OPA1 membrane binding sites in simulations**

153 Upon encountering the membrane surface, the positively charged residues within the MIL region
154 formed the initial charge-charge contacts with the negatively charged headgroups of CL
155 molecules, which was followed by rapid engagement of key tryptophan residues with the
156 membrane and the insertion of the MIL into the bilayer (Fig. 1d). The docking region then formed
157 peripheral interactions with the membrane lipids, positioning the positively charged membrane-
158 facing surface of the PD onto the bilayer. At this stage, the local lipid composition of the membrane
159 patch near the protein contact sites remained unchanged. Concurrently with the insertion of the
160 MIL into the membrane, CL rapidly localized at the protein-membrane contact sites and the
161 number of sidechain-CL interactions increased to ~50% of total contacts, reaching a higher
162 average density compared to POPC and POPE despite its lower concentration in the simulated
163 membrane (Figs. 1c-d). While POPC and POPE transiently interact with S-OPA1 at the
164 membrane contact sites, CL molecules establish much stronger interactions, demonstrated by
165 lipid contact residence times 5 to 10 times longer than the other phospholipids (Fig. 1d).
166 Importantly, control CG MD simulations on the membrane without protein did not exhibit
167 aggregation or phase separation of CL molecules, suggesting that S-OPA1 interactions with the
168 lipid bilayer are the trigger for the recruitment of CL molecules to the protein-membrane contact
169 sites.

170

171 Analysis of the residence times for contacts between protein residues and CL molecules revealed
172 extensive engagement of CL with two specific motifs: MIL residues W771, K772, K773, R774,
173 W775, W778, and R781 and R857 and R858 residues located in the docking region (Fig. 1d).
174 Mutating some of the MIL and docking region residues to alanine within the same CG MD system
175 abolished the membrane binding activity of the tetrameric subassemblies in simulations, and the
176 assemblies remained disengaged in solution while retaining their quaternary structure
177 (Supplementary Fig. S2d). These findings closely mirror our previous observations in

178 experimentally determined structural models. Finally, to confirm the specificity of OPA1-CL
179 interactions, we substituted CL with another negatively charged phospholipid, POPS, in the
180 simulated membrane. These experiments showed short contact residence times for POPS and
181 weaker interactions with OPA1 residues compared to CL (Supplementary Fig. S3a-b). Together,
182 our data suggest that OPA1-membrane interactions are controlled by the two CL binding motifs
183 within the PD of the protein.

184

185 **AA MD simulations confirm local CL accumulation near protein contact sites**

186 While the CG MD simulations already suggest that the positively charged beads of the lysine and
187 arginine residues of the MIL and docking regions engage in contact with the negatively charged
188 beads of CL head group and tryptophan residues of the MIL interact with the hydrophobic tails of
189 lipids, we examined these interactions in greater detail through all-atom (AA) MD simulations. We
190 first extracted one of the subunits of S-OPA1 tetramer 1 and embedded it in a membrane using
191 the membrane-monomer orientations and interactions retrieved from the CG MD simulations. We
192 utilized two separate membrane patches containing two different CL molecular species, CL(18:1)₄
193 and CL(18:2)₄, and ran three replicas of each system for ~1 μ s to facilitate free, unbiased
194 exploration of the protein-lipid contacts. Similar to the CG MD simulations, the AA MD simulations
195 revealed local accumulation of CL around the protein-membrane contact sites in all three replicas
196 of each system, and we did not observe a difference between CL(18:1)₄- and CL(18:2)₄-containing
197 membranes. CL molecules formed constant interactions in particular with the key CL binding
198 motifs of the MIL and docking regions (Figs. 1e-g and Supplementary Fig. S3c-d). While the CG
199 MD simulations displayed high density for the beads of the headgroup and acyl chains of CL,
200 spanning across the OPA1-binding leaflet, the AA MD simulations indicate that only the
201 headgroups contributed to the density in the same leaflet. These differences likely arise from the
202 high flexibility of the CL tails, a feature only captured in the AA MD simulations.

203

204 Despite being only 20% of the membrane composition in all the AA MD simulations, CL accounts
205 for nearly half of the protein-membrane contacts with the membrane-facing residues of the PD
206 (Figs. 1e-g and Supplementary Fig. S3c-d). The key electrostatic interactions between CL and
207 OPA1 are mediated by K772 and R781 of the MIL, R857 and R858 of the docking region, and
208 other critical membrane interface residues, including K800, R824, K847, and R865, within the PD.
209 R857 and R858 residues continue to interact completely peripherally with the CL phosphates via
210 their guanidinium groups on the bilayer surface (Figs. 1e-g and Supplementary Fig. S3c-d). This
211 data shows the preference of positively charged residues located at the membrane interface of

212 S-OPA1 for specific interactions with the negatively charged headgroups of CL molecules,
213 thereby recruiting them to the protein-membrane contact sites. However, there is a greater
214 tendency for the CL molecules to be present in the vicinity of the CL binding motifs (Figs. 1f-g).
215 Analysis of the last 100 ns of each AA MD trajectory reveals an average of ~2 CL molecules in
216 contact with the R857 and R858 residues of the docking region and ~4 CL molecules around the
217 MIL residues, suggesting that CL molecules are particularly enriched around the MIL motif of the
218 PD (Figs. 1f-g and Supplementary Figs. S3c-d).

219
220 The AA MD simulations also revealed enriched hydrophobic contacts between CL and S-OPA1
221 PD near the MIL region. Following the initial protein-membrane contacts, predominantly driven by
222 charge-charge interactions at the solvent-membrane interface, the membrane insertion of the MIL
223 is facilitated by the indole rings of MIL residues W771, W775, and W778. Upon insertion, the
224 tryptophan sidechains become vertically embedded into the spaces in-between lipids, causing the
225 helix comprising the MIL to lodge deep into the membrane by ~10 Å, equivalent to ~25% of the
226 bilayer thickness (Fig. 1f). Mechanistically, the insertion exposes MIL residues to the hydrophobic
227 core of the membrane to facilitate direct interactions with the lipid tails. Interestingly, the three
228 tryptophan residues exhibit less selectivity for the hydrophobic acyl chains of CL upon membrane
229 insertion, forming similar interactions with the acyl chains of POPC and POPE. These findings
230 indicate that charge-charge interactions facilitate the clustering of CL molecules in the vicinity of
231 the PD. Once in close proximity, the CL tails interact with hydrophobic side chains of the MIL,
232 further stabilizing S-OPA1 subunits on the membrane. Collectively, our computational findings
233 demonstrate that the main structural element driving OPA1 activation on CL-containing
234 membranes is the MIL motif, as it facilitates direct binding to CL headgroup and acyl chains, while
235 the docking region plays a lesser role in OPA1-membrane dynamics.

236
237 **S-OPA1 tetramer is capable of bending membranes**
238 In the presence of CL-containing lipid vesicles, S-OPA1 molecules become activated rapidly and
239 polymerize into membrane-remodeling filaments. This process marks the initial step in reshaping
240 the mitochondrial IM, yet the precise stoichiometry of the OPA1 machinery required for initiating
241 local membrane bending remains unknown. As a member of the dynamin superfamily, OPA1
242 functions through the oligomerization of its monomeric, dimeric, or tetrameric basic building blocks
243 into rings or helices to remodel membranes in cells⁵³. Consistent with this notion, our CG MD
244 simulations using S-OPA1 tetramers demonstrate membrane bending in a direction conducive to
245 ring formation of OPA1 proteins on the outer side of the formed tubule (Fig. 1h and Supplementary

246 Fig. S4). Quantitatively, all four tetrameric subassemblies induce positive curvature protruding
247 towards the protein, averaging up to $\pm 0.3 \text{ \AA}^{-1}$ throughout the simulations at specific points where
248 the membrane contacts the protein (Fig. 1h and Supplementary Fig. S4). For comparison, we
249 measured a control membrane without protein and determined an average fluctuation of $\pm 0.03 \text{ \AA}^{-1}$
250 (Fig. 1h). The most curved snapshots of the simulation display local curvature radii ranging from
251 20 nm to 50 nm, a range consistent with the ~19 nm inner lumen diameter observed in our cryoEM
252 structure of the S-OPA1 polymer wrapped around a membrane tube. A lower curvature radius
253 indicates stronger membrane bending, and the deformations observed in CG MD simulations are
254 likely limited by the strong lateral membrane pressure acting through periodic cells, preventing
255 bending of the lipid bilayer. Additionally, S-OPA1 tetramer was able to bend POPS-containing
256 membranes, albeit to a lesser extent (Fig. 1h). Similar bending induced by the protein also takes
257 place with the other tetramers, as presented later in the manuscript.

258

259 **Saturation of CL acyl chains hinders S-OPA1 activity**

260 To test our computational models of OPA1 in biochemical assays, we employed an *in vitro*
261 reconstitution assay using purified S-OPA1 and liposomes prepared with various lipid
262 compositions (Supplementary Figs. S5a-b and Supplementary Table 2). We reconstituted human
263 S-OPA1 WT samples onto lipid bilayers and quantified the membrane binding and remodeling
264 activity of the protein by using co-sedimentation assays and negative-stain transmission electron
265 microscopy (TEM). Consistent with our previous findings, analysis of the reconstitution assays
266 revealed that S-OPA1 molecules fail to bind and polymerize on lipid vesicles when CL is omitted
267 from lipid compositions (Supplementary Fig. S6). Similarly, substitution of CL with negatively
268 charged phospholipids POPG and POPS impaired S-OPA1's ability to remodel membranes
269 (Supplementary Fig. S6). Although we observed some remodeling with POPS-containing
270 liposomes, the total remodeled area was decreased by more than 95% when compared to the
271 experiments with CL-enriched membranes (Supplementary Fig. S6c-d). To investigate the role of
272 CL acyl chain composition on S-OPA1-mediated membrane organization, we comprehensively
273 characterized five different molecular species of CL *in vitro*. We prepared liposomes with two
274 saturated (CL(16:0)₄ and CL(18:0)₄) and three unsaturated (CL(16:0)₂-(18:1)₂, CL(18:1)₄, and
275 CL(18:2)₄) CL species and tested their effect on S-OPA1 activity. We observed the highest
276 amount of membrane binding and remodeling with CL(18:2)₄, which is the most abundant CL
277 species in cardiac and skeletal muscle cells (Fig. 2 and Supplementary Fig. S7). While we
278 detected comparable S-OPA1 membrane binding activity with the CL(16:0)₂-(18:1)₂ and
279 CL(18:1)₄, this activity decreased by ~70% with liposomes containing CL(16:0)₄ and CL(18:0)₄

280 (Figs. 2a-b). Next, S-OPA1-mediated membrane remodeling was measured in reconstitution
281 assays. After 4hrs of reaction, S-OPA1 was able to form higher-order assemblies in the presence
282 of CL(16:0)₂-(18:1)₂, CL(18:1)₄, and CL(18:2)₄, whereas CL(16:0)₄ and CL(18:0)₄ hindered the
283 ability of S-OPA1 to assemble into stable elongated filaments, indicating a clear preference for
284 unsaturated CL species over saturated species for remodeling (Fig. 2c-e and Supplementary Fig.
285 S7). Together, these findings suggest that CL acyl chain composition is critical for the proper
286 assembly and function of OPA1 on lipid membranes. Since CL(18:1)₄ and CL(18:2)₄ are found to
287 be the dominating CL species in various tissues, we conducted the subsequent experiments using
288 these two molecular species of CL.

289
290 **The two CL binding motifs contribute to the membrane remodeling activity of S-OPA1**
291 To verify the functional relevance of the two CL binding motifs, we created, recombinantly
292 expressed, and purified three mutant constructs, as well as the WT construct. An alanine point
293 mutation was introduced to the positively charged R858 residue within the docking region motif.
294 A second mutant construct was generated to replace the charged and hydrophobic MIL region
295 motif (⁷⁷¹WKKRWLYWKNR⁷⁸¹) with a polyalanine stretch, and an R858A-MIL polyalanine double-
296 mutant was employed to show the importance of both CL-binding motifs. While the individual
297 R858A and MIL polyalanine mutants reduced the membrane binding activity by ~12% and ~54%,
298 respectively, the double mutant led to a ~60% decrease in binding. Together, both mutants
299 exhibited reduced membrane binding activity on CL-enriched liposomes compared to the WT
300 (Figs. 3a-b). We then determined that R858A and MIL polyalanine mutations impair S-OPA1's
301 ability to form ordered assemblies and remodel CL-containing lipid membranes *in vitro* (Figs. 3c-
302 f). Notably, the R858A mutant diminished the total remodeled area by approximately 80% and
303 generated more small size filaments, while the MIL region mutant and the double-mutant resulted
304 in abrogation of remodeling function *in vitro* (Figs. 3c-f). Our biochemical data indicate that the
305 two conserved motifs form stable interactions with CL molecules, ensuring the proper assembly
306 of OPA1 polymers on the membrane and promoting mitochondrial morphology remodeling.
307

308 **Structure of S-OPA1 assembly bound to membranes containing contrast-enhancing
309 probes**

310 To experimentally determine CL localization in intact lipid membranes, we synthesized CL with
311 bromine atoms added to the unsaturated fatty acyl chains. This modification capitalizes on the
312 lipophilicity, steric, and enhanced electron scattering properties of Br, and results in dibrominated
313 lipid tails mimicking unsaturated tails that facilitate the determination of the position of CL

314 molecules within the structural organization of lipid bilayers (Fig. 4a and Supplementary Fig.
315 S8)^{54,55}. We reconstituted human S-OPA1 onto lipid bilayers (both vesicles and nanotubes)
316 containing brominated CL and learned that S-OPA1 can self-organize into higher-order structures
317 on these bilayers and induce the protrusions of narrow lipid tubes (Supplementary Fig. S9a). This
318 observation indicates that the brominated CL, which yields stronger electron scattering, exhibits
319 similar membrane packing properties and behaves indistinguishably from unsaturated
320 phospholipids *in vitro*. To measure and model the interactions between CL and OPA1, we
321 prepared samples for cryoEM and recorded images of S-OPA1 filament segments bound to
322 brominated CL-containing lipid tubes using a 300-kV Krios cryoEM microscope (Supplementary
323 Fig. S10 and Supplementary Table 1). Image segments were first aligned and averaged to obtain
324 *ab initio* 3D reconstructions, followed by 3D classification to generate well-ordered subsets using
325 the Relion software (Supplementary Figs. S10 and S11)⁵⁶. However, the membrane-bound
326 assemblies exhibited slightly variable tubule diameters, hindering coherent inter-tube averaging
327 and resulting in multiple conformational classes. To address this variability, we performed 3D
328 classification without alignment and identified filament segments with nearly uniform diameters.
329 The best quality maps were then refined to obtain a sub-nanometer reconstruction of S-OPA1
330 polymer bound to brominated lipid membranes (Supplementary Fig. S11). The density map
331 distinctly delineates two components corresponding to the protein coat and lipid bilayer, with
332 numerous S-OPA1 subunits forming a spiraling homomeric filament on membranes (Fig. 4 and
333 Supplementary Fig. S10). This reconstruction represents the membrane-proximal conformation
334 of the OPA1 assembly, wherein the PD is docked on the membrane surface and the MIL is
335 embedded in the lipid bilayer (Figs. 4b-d).

336
337 The final 3D reconstruction of the membrane-bound S-OPA1 polymer reveals an outer diameter
338 of 48.4 nm and an inner lumen diameter of 19.1 nm (Fig. 4d). It exhibits a three-start helical
339 structure with a rise of 7.69 Å and a twist of 128.642 degrees, with minimal intersubunit
340 connectivity arising from the low packing density of the S-OPA1 lattice (Figs. 4b-c, Supplementary
341 Figs. S10 and S11, and Supplementary Table 1). The cryoEM density map achieved sufficient
342 resolution to unambiguously assign the orientation of the S-OPA1 domains. While the bundle-
343 signaling element (BSE), stalk, and PD could be resolved, the distal GTPase domains that are
344 not interacting with the lipid bilayer were at the lower local resolution, indicating the dynamic
345 nature and conformational flexibility in the membrane-bound state (Supplementary Fig. S10d).
346 Nonetheless, leveraging this reconstruction and prior structural knowledge enabled us to build
347 precise molecular models of S-OPA1 tetramers bound to brominated lipid membranes with an

348 overall resolution of 6.4 Å (Fig. 4 and Supplementary Figs. S10 and S11). A comparison of
349 membrane-bound OPA1 models from native and brominated liposomes showed highly similar
350 structures with a root-mean-square deviation (RMSD) of only 0.78 Å over 698 Ca atoms of the
351 protein (Supplementary Fig. S10e). These findings collectively indicate that bromine labeling of
352 CL acyl chains does not induce notable structural changes in how OPA1 assembles on lipid
353 membranes.

354

355 **CryoEM structure shows CL enrichment in the OPA1-bound outer leaflet**

356 To detect the position of CL molecules in the reconstructions, we investigated the membrane
357 layer of the experimental density map for focal enrichment of CL-Br. Initially, we normalized the
358 pixel value distributions to the S-OPA1 intensity from radial averages and obtained horizontal and
359 vertical slices of brominated and non-brominated reconstructions (Figs. 4d-f). The density map
360 confirmed that the docking and the MIL regions of the PD are positioned to make direct
361 interactions with CL molecules in the lipid bilayer (Figs. 4d-e). Comparing the Coulombic
362 potentials from the resulting 3D maps of unlabeled versus labeled membrane tubes, we located
363 the surplus signals attributable to halogen scattering in the outer leaflet (Figs. 4f-g). Although CL-
364 Br enrichment in the OPA1-bound leaflet was observed, the bilayers remained compositionally
365 heterogeneous with CL-Br distributed throughout the bilayers as observed in the difference map
366 between the CL membrane and CL-Br membrane (Figs. 4f-g and Supplementary Fig. S10f). In
367 CG MD simulations, CL molecules form frequent microsecond-timescale interactions with the
368 membrane-facing residues of OPA1 PD. Thus, the combined experimental and computational
369 data imply a dynamic nature of CL within lipid bilayers, which is critical for OPA1 anchoring. These
370 results collectively demonstrate that halogenated lipids scatter electrons strongly, enabling the
371 quantitative localization of surplus scattering in our cryoEM maps for estimating the changes in
372 CL concentration within each leaflet. Additionally, identifying overall enrichment of CL in the outer
373 leaflet with cryoEM supports our CG MD data, providing us a platform to further explore the
374 mechanics governing mitochondrial membrane reshaping at higher resolution.

375

376 **MLCL forms similar clusters near protein-membrane contact sites.**

377 Next, we investigated whether the accumulation of MLCL in lipid bilayers affects OPA1's ability to
378 reshape membranes and control the dynamic architecture of mitochondria. We utilized CG MD
379 simulations with the same four S-OPA1 tetramers and assessed how the replacement of CL by
380 MLCL affects OPA1's interactions with membranes. All parameters and the overall setup
381 remained identical to the previous CG MD simulations, except for the substitution of CL with

382 MLCL. After >8μs of simulations, all replicas of the trajectories for the four models revealed
383 membrane binding and clustering of MLCL around the same CL binding motifs. Additionally, they
384 exhibited similar protein-lipid interaction profiles and residence times compared to CL contacts.

385
386 To quantitatively analyze the MLCL-protein interactions, we measured the residence times of
387 MLCL in the presence of S-OPA1 tetramers and compared them to the CL residence times. Within
388 the uncertainty of the sampling in the CG MD simulations, residence times for protein-lipid
389 contacts were similar between MLCL and CL, and both residence times were larger than those
390 observed for negatively charged POPS in control experiments (Supplementary Fig. S3a).
391 Likewise, MLCL- and CL-containing lipid bilayers displayed a similar number of protein-lipid
392 contacts per residue in AA MD simulations, despite MLCL containing one fewer acyl chain
393 (Supplementary Fig. S3b). Collectively, our MD simulations at CG and AA resolutions revealed
394 no major differences in how human OPA1 interacts with membranes containing CL or MLCL.

395
396 **MLCL accumulation impairs OPA1's ability to bend and remodel membranes**
397 Despite the similar protein-lipid interactions and residence times observed with MLCL and CL in
398 the bilayers, the deformation experienced by the MLCL-containing membranes is substantially
399 weaker in the simulations, especially for assemblies mediated by the conserved crisscross
400 association of S-OPA1 monomers (tetramers 1 and 3) (Fig. 5a and Supplementary Fig. S4). The
401 simulations suggest that differences in the spontaneous curvature and other material properties
402 of CL and MLCL are critical for OPA1-mediated membrane remodeling, with CL enabling
403 membrane shape plasticity and bilayer deformation upon protein binding. Furthermore, S-OPA1
404 can also warp POPS-containing membranes to some extent (Fig. 1h and Supplementary Fig. S6),
405 indicating that the intrinsic mechanical properties of lipid bilayers may play an important role in
406 governing OPA1's ability to remodel membranes.

407
408 To experimentally probe the mechanistic basis of MLCL interactions with human OPA1, we
409 performed co-sedimentation experiments with S-OPA1 and liposomes containing increasing
410 concentrations of MLCL in place of CL (Supplementary Fig. S9b and Supplementary Table 2).
411 Consistent with MD simulations, increasing concentrations of MLCL resulted in only very minor
412 differences in OPA1's ability to bind liposomes. We found that the presence of 1% to 5% of MLCL
413 in liposomes resulted in similar membrane binding activity for S-OPA1 compared to liposomes
414 containing 25% CL (Figs. 5b-c). Increasing MLCL concentration to 25% diminished S-OPA1's
415 ability to bind liposomes, resulting in a ~30% decrease in membrane binding (Figs. 5b-c). The

416 major difference in the chemical structure of MLCL is the absence of a single acyl chain compared
417 to CL. The results of our MD simulations and co-sedimentation assays indicate that while the
418 changes in the acyl chain content of CL molecular species do not affect the recruitment of OPA1
419 to the lipid membranes at low molar concentrations, the full replacement of CL by MLCL
420 decreases the membrane binding activity of the protein.

421

422 Following this, we investigated the impact of MLCL on the membrane remodeling activity of S-
423 OPA1. We reconstituted S-OPA1 with CL- and MLCL-containing liposomes and monitored the
424 protein's oligomerization and membrane remodeling activity using negative-stain TEM imaging
425 (Fig. 5d). While the reconstitution of S-OPA1 on CL-containing liposomes resulted in the formation
426 of higher-order protein assemblies and further tubulation of membranes, the replacement of CL
427 by MLCL hindered the liposome remodeling activity of the protein and resulted in more than 90%
428 decrease in total remodeled area (Figs. 5d-g). Lowering MLCL concentrations to 1 to 5% in the
429 lipid compositions still reduced the membrane remodeling ability of S-OPA1 by more than 50%
430 and the activity of the protein was not recovered. This suggests that even the lower molar
431 concentrations of MLCL in lipid bilayers are enough to interrupt OPA1 polymerization on
432 membranes, which is detrimental to OPA1-mediated mitochondrial remodeling (Figs. 5d-g).
433 Finally, we reconstituted S-OPA1 on membrane nanotubes containing increasing concentrations
434 of MLCL (1 to 10%) and determined that MLCL accumulation does not alter the formation of
435 higher-order S-OPA1 assemblies on pre-curved membranes *in vitro* (Supplementary Figs. S9c-
436 d). This suggests that the presence of MLCL increases the energy barrier required for local
437 membrane bending.

438

439 Overall, while we did not observe notable reductions in how OPA1 binds CL- and MLCL-
440 containing lipid bilayers, membrane remodeling experiments demonstrated that the presence of
441 MLCL in lipid bilayers alters the remodeling activity of OPA1 machinery. Our findings suggest that
442 MLCL accumulation changes the malleability of the lipid bilayer and restricts OPA1's ability to
443 remodel membranes. Hence, we postulate that OPA1 relies on the lipid composition of
444 mitochondrial membranes for its activity, which is precisely tuned by the unique properties of CL
445 and its enrichment at the OPA1-membrane contact sites.

446

447 In our proposed mechanism, OPA1 proteins are recruited to the membrane via specific
448 interactions with CL molecules, which are randomly distributed throughout the membrane with
449 potential pre-formed patches enriched in CL within the lipid bilayer. Upon protein binding, CL

450 molecules rapidly localize to the outer leaflet of the bilayer near the two CL binding motifs,
451 facilitating the formation of stable interactions between OPA1 and lipid bilayers. At these CL-rich
452 contact sites, unique structural properties of CL and its stable interactions with key OPA1 residues
453 allow for membrane deformation. Concomitantly, by leveraging these specific CL contacts, OPA1
454 proteins form higher-order assemblies required for the remodeling and the fusion of the
455 mitochondrial IM. The partial replacement of CL by MLCL, even at low concentrations, makes the
456 membrane less prone to bending, which in turn disrupts OPA1 activity, thereby hindering
457 membrane remodeling mechanisms (Fig. 6).

458

459 **Discussion**

460 Here, we performed multiple CG and AA MD simulations to explore the lipid-lipid and lipid-protein
461 interactions driving OPA1-mediated mitochondrial remodeling. These simulations were set up
462 with various OPA1 structures and the membrane bilayer mimicking the lipid composition of the
463 mitochondrial IM. Dynamic models generated through these simulations revealed the CL
464 dynamics within the bilayer, exhibiting enrichment in the outer leaflet and extensive contacts with
465 OPA1 residues. Furthermore, our computational approach enabled us to accurately measure the
466 lateral chemical organization and morphological changes in CL-enriched membranes that often
467 occur at shorter time and length scales and are challenging to probe experimentally at the
468 molecular level. These analyses led to the identification of two highly conserved binding motifs
469 located at the MIL and docking regions of the PD, showcasing strong interactions with CL
470 molecules within intact lipid membranes (Supplementary Figs. S3c-d and S5c). The CL binding
471 motifs establish critical electrostatic and hydrophobic interactions with both the headgroup and
472 acyl chains of CL, reminiscent of protein complexes observed in oxidative phosphorylation^{23,24},
473 and thereby facilitate membrane remodeling. As anticipated, mutations of the key residues to
474 alanine hindered the membrane binding and remodeling activity of OPA1 in our computational
475 and biochemical assays. Note that our reconstitution assays and MD simulations offer an
476 approximation of biological membranes. Moreover, our results align with previous studies,
477 demonstrating that mutations to membrane-interacting residues of OPA1 result in fragmented
478 mitochondrial morphology in living cells^{10,11}. Overall, these findings allowed us to pinpoint specific
479 lipid-protein interactions and understand how CL regulates the activity of OPA1 to maintain
480 mitochondrial homeostasis.

481

482 CL is a pivotal regulatory lipid playing critical roles in various mitochondrial processes, including
483 energy production, apoptosis, mitophagy, oxidative stress, and mitochondrial fusion and fission,
484 which govern mitochondrial shape and function. Yet, for many of these cellular processes, it is
485 currently unknown how the role of CL extends from maintaining membrane structure to an intimate
486 association with mitochondrial proteins. Central to these processes is the intricate interplay
487 between CL and the OPA1 protein that results in the initiation of OPA1-mediated mitochondrial
488 membrane remodeling and maintenance of a healthy organellar network distributed throughout
489 the cell. Thus, CL assumes a direct and regulatory role in the structural and functional remodeling
490 of mitochondria.

491

492 The most distinguishing features of CL are its dimeric structure and polymorphic phase
493 behavior^{57–59}. CL and unsaturated phosphatidylethanolamine have the ability to organize into non-
494 lamellar phases, particularly the hexagonal II phase, to promote local structures, such as negative
495 curvatures, within membranes^{16,33–36,39}. Previous studies reported that in the absence of divalent
496 cations, CL prefers the lamellar phase at physiological temperature to form an extended bilayer.
497 Ca²⁺ promotes tighter packing of CL headgroups and can induce a geometry that favors the
498 hexagonal phase^{57–59,65,66}. We found that CL is also highly dynamic and can diffuse near protein
499 contact sites within microseconds throughout the simulated bilayer. Surprisingly, our simulations
500 revealed that CL forms multiple short-lived interactions with the OPA1 side chains at the CL
501 binding motifs rather than long-lived, stable interactions to modulate the formation of the OPA1
502 scaffold for membrane remodeling. Together, these findings suggest that both the polymorphic
503 phase behavior and the rapid lateral diffusion of CL within the bilayer play a crucial role during
504 membrane shape transitions.

505

506 Determining the functional role of CL within the structural framework of intact lipid bilayers poses
507 challenges due to the heterogeneity and dynamic nature of mitochondrial membranes. Prior
508 research has demonstrated that brominated and iodinated lipids behave similarly to their native
509 counterparts and can serve as contrast-enhancing probes to delineate specific lipids within
510 membranes^{54,55}. Moreover, the utilization of bromo-substituents on aliphatic double bonds has a
511 well-established history as fluorescence quenchers in model membranes^{67–69}. By labeling CL with
512 halogen atoms, which scatter electrons more strongly than acyl chains alone, we quantitatively
513 located the surplus scattering in our cryoEM maps and estimated the concentration of CL within
514 each leaflet. Our observations of the OPA1 structure bound to brominated membranes provide
515 experimental evidence that CL is enriched in the OPA1-binding leaflet to promote the remodeling
516 of mitochondrial membranes. We anticipate that this versatile tool will prove instrumental in
517 determining how CL either activates or inhibits other key membrane-associated processes in the
518 regulation of mitochondrial morphology and function.

519

520 On the other hand, human OPA1 forms several homo- and heterotypic interactions with proteins
521 and lipids to modulate the dynamic remodeling of mitochondrial network^{49,70–74}. In addition to its
522 key interactions with CL, the interplay between L-OPA1 and S-OPA1 is crucial for controlling
523 mitochondrial IM fusion and cristae dynamics. Previously, it was shown that L-OPA1 can tether
524 and hemifuse bilayers but is unable to transition through the final step of pore opening or mediate
525 low levels of pore opening⁵¹. Hence, optimal fusion requires a combination of L-OPA1 and S-

526 OPA1 together, which synergistically catalyzes efficient and fast membrane pore opening^{51,75}.
527 Other studies reported that L-OPA1 alone does not have a notable fusion activity under normal
528 cellular conditions but becomes more fusogenic under specific cell stress conditions⁷⁶. Finally, L-
529 OPA1 was shown to be sufficient to mediate fusion in cells lacking the proteases (YME1L and
530 OMA1) responsible for generating S-OPA1^{48,49}. It appears that the heterotypic OPA1 fusion
531 machinery has a complex regulatory mechanism, and the relative contribution of L- versus S-
532 OPA1 to membrane remodeling and fusion remains incompletely understood. L-OPA1 and S-
533 OPA1 vary only by a short transmembrane helix (residues 88-109) and a linker region (residues
534 110-195). We postulate that the linker region provides sufficient structural freedom for membrane-
535 anchored L-OPA1 to form higher-order structures analogous to those we observe for S-OPA1,
536 and for L-OPA1 and S-OPA1 to co-assemble.

537
538 Barth syndrome (BTHS) stands as a significant X-linked cardiomyopathic disease characterized
539 by perturbations of cardiolipin (CL) metabolism in mitochondria^{31,32}. Despite its prevalence, the
540 precise repercussions of altered lipid content underlying BTHS symptoms remain unclear. Here,
541 we sought to determine how loss of CL content and accumulation of MLCL in mitochondrial
542 membranes influence the activity of the key membrane remodeling enzyme, OPA1. Human OPA1
543 governs mitochondrial shape, cristae integrity, and functional output for a vast array of essential
544 metabolic pathways and processes that determine cell function and fate. Initially, we investigated
545 the impact of MLCL accumulation on OPA1-membrane interactions via MD simulations and
546 measured the dynamics of the lipids throughout the bilayer to determine how MLCL molecules
547 engage with OPA1 in the bilayer. Our simulations with CL-enriched membranes demonstrated
548 that even though the CL molecules continuously diffuse throughout the membrane, they
549 frequently associate with the two CL binding motifs. For instance, the interactions between the
550 key binding motif residues W775 and R858 and CL persisted for 1 μ s to 1.5 μ s in residence times.
551 We observed similar S-OPA1-membrane contacts when CL was replaced with MLCL in lipid
552 compositions and measured comparable MLCL residence times for most of the MIL and docking
553 region binding motif residues. This outcome is unsurprising, given that the main components
554 mediating the initial protein-membrane interactions are the membrane-facing lysine and arginine
555 residues of the PD and negatively charged glycerophosphate headgroups of CL and MLCL. The
556 initial steps are followed by the MIL insertion in the membrane, which is mediated by the
557 tryptophan residues within the MIL and their subsequent association with the hydrophobic acyl
558 chains of phospholipids sharing similar physicochemical properties. However, the presence of
559 MLCL hindered OPA1's ability to bend membranes in MD simulations. Further probing of

560 mechanistic links between MLCL and OPA1 activity through biochemical assays confirmed that
561 the replacement of CL with MLCL reduces OPA1's ability to remodel membranes. In these
562 assays, S-OPA1 was able to bind and remodel the membranes that contained increasing MLCL
563 concentrations, but the remodeling activity of the protein was decreased compared to the CL-
564 enriched lipid bilayers. Interestingly, even partial replacement of CL with low molar concentrations
565 of MLCL in membranes restricted the membrane-shaping activity of OPA1. Together, these
566 findings indicate that MLCL accumulation could influence mitochondrial membrane properties,
567 and the regulation of the mitochondrial IM morphology and associated cellular processes by
568 human OPA1 depends on the lipid composition of the lipid bilayers.

569

570 Understanding the intrinsic mechanical properties of CL and MLCL, as well as their interactions
571 with mitochondrial proteins, is critical for determining the molecular basis of pathologies
572 associated with MLCL accumulation⁷⁷. Notably, CL is well known to both facilitate membrane
573 bending to produce positive curvature and to partition into negatively curved regions⁷⁸⁻⁸¹. The
574 distinctive feature of MLCL is the absence of an acyl chain, which induces drastic differences in
575 bilayer mechanical properties and curvature-dependent partitioning behavior⁷⁷⁻⁷⁹. More
576 specifically, MLCL prefers a lamellar phase due to its cylindrical cone shape and induces less
577 membrane curvature. The differences in the chemical structure could also influence the
578 conformation of acyl tails and the accessibility of the headgroup due to hydrogen bonding with
579 the additional hydroxyl group in MLCL, thereby affecting lipid conformations in the vicinity of
580 MLCL. Hence, membranes containing increased concentrations of MLCL would be less malleable
581 by membrane-shaping proteins, including human OPA1. Additionally, membrane binding and
582 remodeling are interconnected processes occurring at different regulatory steps that modulate
583 OPA1 activity. It is plausible that moderate differences in membrane binding could have drastic
584 effects on the more energy-demanding membrane remodeling steps. Overall, these findings
585 indicate that MLCL-containing membranes exhibit greater resistance to protein-mediated shape
586 changes and provide insights into the disruptive effects of MLCL accumulation on mitochondrial
587 membrane dynamics and function.

588

589 Despite the longstanding recognition of the significance of CL in modulating mitochondrial
590 morphology and function, the precise mechanisms through which CL regulates these essential
591 cellular machines, as well as the impact of the MLCL accumulation on mitochondrial membrane
592 remodeling, remain unclear. Our findings highlight how CL molecules cluster near the membrane-
593 binding surfaces of OPA1's PD, engaging in charged and hydrophobic interactions with the

594 conserved CL binding motifs to modulate the activity of the membrane-remodeling enzyme.
595 Moreover, we describe how MLCL build-up in lipid membranes disrupts OPA1's ability to remodel
596 membranes, potentially playing an important role in the pathogenesis of inherited disorders, such
597 as Barth Syndrome. These insights provide a critical structure-function foundation for
598 understanding the mechanisms connecting CL and regulation of mitochondrial morphology, thus
599 establishing a molecular basis for shaping the mitochondrial IM in health and disease.
600

601 **Materials and Methods**

602 **Cloning, expression, and purification.**

603 The gene fragment corresponding to S-OPA1 (Addgene plasmid ID: 26047; residues 252-960)
604 was subcloned into the pCA528 vector, incorporating an N-terminal 10X His tag followed by a
605 SUMO solubility tag. S-OPA1 mutations were engineered using a modified QuickChange
606 Mutagenesis protocol and confirmed through Sanger Sequencing. All S-OPA1 variant constructs
607 were transformed into BL21 DE3-RIPL competent cells. A single colony from each transformation
608 was inoculated into lysogeny broth (LB) media (100 ml) and was grown overnight at 37 °C with
609 kanamycin (50 µg mL⁻¹) and chloramphenicol (25 µg mL⁻¹). The overnight culture (10 ml) was
610 used to inoculate a 750 ml culture of ZYP-5052 auto-induction media and was grown at 37 °C
611 until the optical density at 600 nm (OD₆₀₀) reached a value between 0.6 and 0.8. At this point, the
612 temperature was reduced to 18 °C within the shaker, and cultures continued to grow overnight for
613 an additional 16 hours. Following the 16-hour induction period, the cells were harvested via
614 centrifugation and stored at -80 °C.

615

616 The frozen bacterial pellets were thawed, resuspended with lysis buffer (50 mM HEPES-NaOH,
617 pH 7.5, 500 mM NaCl, 20 mM imidazole, 5 mM MgCl₂, 5 mM CHAPS (Anatrace), 5 mM 2-
618 mercaptoethanol, 10% (v/v) glycerol) supplemented with 0.5% Triton X-100, 0.5 mg DNaseI, 1X
619 EDTA-free complete protease inhibitor cocktail (Roche), and lysozyme. The cells were then lysed
620 using an Emulsiflex C3 homogenizer or a probe sonicator (Qsonica Q500). To remove the cell
621 debris, the lysate was centrifuged at 35,000 x g for 45 minutes at 4 °C. Meanwhile, a Ni-NTA
622 (Qiagen) affinity column was equilibrated with lysis buffer. The supernatant was then filtered
623 through a 0.45 µm membrane (Millipore) and transferred to a column, where it was incubated with
624 the Ni-NTA beads on a roller for 1 hour at 4 °C. The column was then washed with 10 column
625 volumes (CV) of lysis buffer followed by 10 CVs of high salt buffer (50 mM HEPES-NaOH, pH
626 7.5, 1 M NaCl, 20 mM imidazole, 5 mM MgCl₂, 5 mM CHAPS, 5 mM 2-mercaptopethanol, and 10%
627 (v/v) glycerol) and high imidazole buffer (50 mM HEPES-NaOH, pH 7.5, 500 mM NaCl, 80 mM
628 imidazole, 5 mM MgCl₂, 5 mM CHAPS, 5 mM 2-mercaptopethanol, and 10% (v/v) glycerol) washes.
629 The sample was then eluted with 10 CVs of elution buffer (50 mM HEPES-NaOH, pH 7.5, 500
630 mM NaCl, 500 mM imidazole, 5 mM MgCl₂, 5 mM CHAPS, 5 mM 2-mercaptopethanol, and 10%
631 (v/v) glycerol). Following elution, the N-terminal 10XHis-SUMO tag was cleaved using the Ulp1
632 enzyme while dialyzing against the FPLC buffer (50 mM HEPES-NaOH, pH 7.5, 500 mM NaCl, 5
633 mM MgCl₂, 5 mM CHAPS (Anatrace), 5 mM 2-mercaptopethanol, 10% (v/v) glycerol) at 4 °C. The
634 digested protein samples were then concentrated with an Amicon Ultra (Millipore) concentrator

635 (50 kDa MWCO) and subjected to further purification using a Superdex-200 16/60 column (Cytiva)
636 equilibrated with the FPLC buffer for further purification. Pure fractions were pooled, concentrated
637 to 2 mg mL⁻¹, aliquoted, flash-frozen with liquid nitrogen, and stored at -80 °C for further use.

638

639 **Preparation of lipid vesicles and nanotubes.**

640 All lipids, except for brominated cardiolipin (CL-Br), were purchased from Avanti Polar Lipids.
641 Stock solutions were prepared by dissolving lipids in a chloroform, methanol, and water mixture
642 (20:9:1, (v/v/v)) and stored in glass vials at -20 °C. The lipids in this study, 1-palmitoyl-2-oleoyl-
643 glycero-3-phosphocholine (POPC), 1-palmitoyl-2-oleoyl-sn-glycero-3-phosphoethanolamine
644 (POPE), 1-palmitoyl-2-oleoyl-sn-glycero-3-phospho-L-serine (POPS), 1-palmitoyl-2-oleoyl-sn-
645 glycero-3-phospho-(1'-rac-glycerol) (POPG), L-a-lysophosphatidylinositol (Soy Lyso PI), 1',3'-
646 bis[1,2-dipalmitoyl-sn-glycero-3-phospho]-glycerol (CL (16:0)₄), 1',3'-bis[1,2-distearoyl-sn-
647 glycero-3-phospho]-glycerol (CL (18:0)₄), 1',3'-bis[1-palmitoyl-2-oleoyl-sn-glycero-3-phospho]-
648 glycerol (CL(16:0)₂(18:1)₂), (1',3'-bis[1,2-dioleoyl-sn-glycero-3-phospho]-glycerol (CL (18:1)₄),
649 heart CL (CL (18:2)₄), and monolyso-cardiolipin (MLCL (94.6% (18:2)₃ and 2.6% (18:1)₃) were
650 used as purchased without any modification. CL-Br was prepared by adapting previously
651 described procedures for brominating alkenes in the lipids (54, 57). Briefly, CL was dissolved in
652 5 mL of chloroform (ACS grade) and placed in a scintillation vial on ice. Liquid bromine,
653 stoichiometric to the number of double bonds (Sigma Aldrich), was slowly added dropwise while
654 the lipid solution was stirred on ice. The vial was then sealed and stirred on ice for 30 minutes in
655 the dark. Solvent and excess bromine were removed under vacuum overnight, and the product
656 was stored under a nitrogen atmosphere at -80 °C. The presence of bromine atoms on CL was
657 confirmed with mass spectrometry (Supplementary Figs. S8a-b) and nuclear magnetic resonance
658 (NMR) (Supplementary Figs. S8c-d). Before use, the CL-Br was warmed to room temperature
659 and dissolved in chloroform to 5 mg mL⁻¹. A lipid mixture of 45% POPC, 22% POPE, 8% PI, and
660 25% CL was used to prepare lipid vesicles mimicking the lipid composition of the mitochondrial
661 inner membrane (IM)⁸². Conversely, CL-enriched lipid nanotubes were prepared using a lipid ratio
662 of 90% D-galactosyl-(β)-1,1'N-nervonoyl-D-erythro-sphingosine (C24:1 Galactosyl(β) Ceramide,
663 GalCer), and 10% CL or CL-Br. The other lipid compositions used in this study are provided in
664 Supplementary Table 2. Vesicles and nanotubes were prepared following an established
665 protocol²⁵. Lipid stock solutions were warmed to room temperature for 15 minutes before they
666 were mixed in a glass vial. The lipid mixtures were dried under a stream of nitrogen with rotation,
667 and residual chloroform was further evaporated under vacuum overnight. The lipid film was
668 resuspended in liposome buffer containing 20 mM HEPES-NaOH, pH 7.5, and 150 mM NaCl and

669 rehydrated via vortexing. Unilamellar vesicles were prepared by extruding the rehydrated lipid film
670 through a 50 nm pore-size polycarbonate membrane (Avanti), flash-frozen in liquid nitrogen,
671 aliquoted, and stored at -80 °C. Lipid nanotubes were resuspended in liposome buffer with
672 vortexing, sonicated with a bath-sonicator at 50 °C for 3-5 minutes until the lipid clumps were
673 dissolved, and were used immediately.

674

675 **Reconstitution assays and negative-stain transmission electron microscopy (TEM).**

676 To set up reconstitution assays, the protein samples were further purified using a Superose 6
677 Increase 10/300 GL column (Cytiva) equilibrated with the reaction buffer (20 mM HEPES-NaOH,
678 pH 7.5, 130 mM NaCl, 10 mM KCl, 2 mM MgCl₂, 2 mM DTT, and 2% (v/v) glycerol). Purified
679 samples (1.6 to 6 µM) were reconstituted with various liposomes and lipid nanotubes (Table S2)
680 in the presence of 500 µM β,γ-methyleneguanosine 5'-triphosphate sodium salt (GMPPCP) for 4
681 hours at room temperature. Reconstituted samples were applied onto a glow-discharged metal
682 mesh grid coated with carbon and stained with uranyl formate (0.75% w/v). Samples were
683 visualized using negative-stain TEM. Images were collected on a Tecnai T12 Spirit TEM operating
684 at 100 kV and equipped with an AMT 2k x 2k side-mounted CCD camera. Most images were
685 recorded at a nominal magnification of 98,000x with a calibrated pixel size of 6.47 Å/pixel.
686 Additional TEM micrographs were collected on a 120 kV Talos L120C TEM (Thermo Fisher
687 Scientific) equipped with a Gatan 4k x 4k OneView camera at 17,500x magnification (pixel size,
688 8.4 Å/pixel). All experiments were performed in triplicate, and error bars indicate the standard
689 error of the mean (s.e.m.).

690

691 **Liposome co-sedimentation assays.**

692 Purified wild-type or mutant S-OPA1 proteins were buffer exchanged into the liposome buffer (20
693 mM HEPES-NaOH, pH 7.5, and 150 mM NaCl) using micro-spin desalting columns (Thermo
694 Scientific Zeba). Equal volumes (25 µl) of protein (0.2 to 0.25 mg ml⁻¹) and unilamellar vesicles
695 (1.0 mg ml⁻¹) were then mixed and incubated at room temperature for 30 min. After incubation,
696 the samples were centrifuged at 55,000 rpm for 30 min at 20 °C using a TLA-120.2 rotor (Beckman
697 Coulter). Reaction mixtures containing liposomes without CL were centrifuged at 85,000 rpm for
698 30 min to pellet proteoliposomes. The resulting supernatant and pellet fractions were subjected
699 to SDS-PAGE analysis, and gel bands were quantified using ImageJ software⁸³. Lipid
700 compositions used in co-sedimentation assays are listed in Supplementary Table 2. All
701 experiments were performed in triplicate, and error bars indicate the standard error of the mean
702 (s.e.m.).

703

704 **CryoEM grid preparation and data collection.**

705 For cryoEM, 6 μ l of membrane reconstitution reaction containing lipid nanotubes with CL-Br was
706 pipetted onto glow-discharged R1.2/1.3 200 copper mesh grids (Quantifold) in 100% humidity at
707 10 °C, incubated for 30 seconds, and blotted with a blot force of 0 for 4 seconds using a Vitrobot
708 Mark IV (FEI). The grids were then plunge frozen into liquid ethane and stored under liquid
709 nitrogen until imaged. Micrographs were acquired on a Titan Krios TEM (Thermo Fisher Scientific)
710 operated at 300 kV and equipped with a K3 direct electron detector (Gatan) and a GIF Quantum
711 energy filter (Gatan) with a slit width of 20 eV. SerialEM software⁸⁴ was used for data acquisition.
712 A total of 4,640 movie stacks were acquired with a defocus range of 0.5 to 1.5 μ m at a nominal
713 magnification of 105,000x, corresponding to a 0.417 Å/pixel in super-resolution mode. The movies
714 were dose-fractionated into 118 frames with ~0.55 e⁻ per Å⁻² per frame and a total exposure time
715 of 6 s, resulting in an accumulated dose of ~65 e⁻Å⁻² for each stack.

716

717 **CryoEM data processing and 3D Reconstruction.**

718 Data processing procedure for membrane-bound OPA1 filaments was previously described¹⁰.
719 Briefly, motion-corrected movies were imported into RELION 4.0⁵⁶, and contrast transfer function
720 (CTF) parameters were determined using CTFFIND4⁸⁵. Following manual filament picking, a total
721 of 233,341 segments were extracted from 4,640 micrographs with the data 2x binned by Fourier
722 cropping (1.668 Å/pixel) and were subjected to multiple rounds of 2D and 3D classification,
723 resulting in a subset of 11,469 particles. The resulting class was then subjected to 3D auto-
724 refinement using a protein-only soft mask. Successive rounds of refinement were performed with
725 higher resolution reference maps obtained after CTF and aberration refinements, which improved
726 the map resolution to 6.7 Å. The helical parameters were refined to a rise of 7.69 Å and a twist of
727 128.642° per subunit. To further improve the signal-to-noise ratio, each independent half-map
728 was segmented, resampled on a common grid, and summed according to the C2 symmetry axis
729 of the OPA1 dimer using UCSF Chimera⁸⁶. These summed unfiltered half maps were used during
730 the post-processing step, yielding a final reconstruction at 6.4 Å resolution. The resolution of the
731 final reconstructions was estimated by the Fourier Shell Correlation (FSC) between the two
732 independent half maps at FSC=0.143. Resolution-dependent negative B-factors were applied to
733 all final reconstructions for sharpening. Local resolution estimations were calculated using
734 ResMap⁸⁷. All cryo-EM data processing and analysis software was compiled and supported by
735 the SBGrid Consortium⁸⁸. An overview of cryo-EM data collection and image processing statistics
736 was provided in Supplementary Fig. S11.

737

738 **Model building, refinement, and validation.**

739 The cryoEM structure of membrane-bound S-OPA1 polymer (PDB ID: 8CT1) served as an initial
740 reference for model building and refinement. Two distinct tetrameric models were extracted from
741 the polymeric assembly and manually fitted into the density map using Chimera⁸⁶. The tetrameric
742 models underwent iterative refinement against the cryoEM map with global minimization, local
743 grid search, and B factor refinement along with secondary structure, Ramachandran, and rotamer
744 restraints to improve the model-map correlation coefficient using the phenix.real_space_refine
745 tool in the PHENIX software package⁸⁹. Further corrections to the models were made in Coot⁹⁰
746 with torsion, planar peptide, and Ramachandran restraints. The quality of the model
747 stereochemistry was validated by PHENIX and MolProbity⁹¹, and the model refinement and
748 validation statistics are summarized in Supplementary Table 1. All structural figures were
749 prepared in VMD⁹².

750

751 **Molecular dynamics simulations.**

752 CryoEM structures of membrane-bound S-OPA1 polymers (PDB IDs: 8CT1 and 8CT9) were used
753 as starting monomeric and tetrameric models for both CG and AA MD simulations. All MD
754 simulation systems were set up using modules of the CHARMM-GUI server⁹³, and then
755 minimized, equilibrated, and run for production using standard CHARMM-GUI procedures, using
756 Gromacs 2022⁹⁴. Coarse-grained systems were prepared with MARTINI22p parameters and
757 elastic networks^{95,96} for POPC, POPE, POPS, and CL, all inside the corresponding CHARMM-
758 GUI module⁹⁷, except for manual building and parametrization of MLCL membranes, which along
759 with AA MD simulation files were kindly provided by Dr. Eric May, and described previously⁷⁹. The
760 dimensions of membranes for CG simulations were sized around 30nm x 30nm x 27nm, reaching
761 around 1 million beads, which represent ~10 million atoms in each system. MARTINI simulations
762 were run for production at 303 K and 1 atm following minimization and thermal equilibration by
763 using the standard procedures and parameters as provided by CHARMM-GUI. Briefly, a standard
764 semi-isotropic Berendsen barostat was used for equilibration while progressively releasing
765 positional restraints on the protein, and a standard Parrinello-Rahman semi-isotropic barostat was
766 used without restraints. The integration timestep during production was 20 fs. The simulations
767 were run for at least ~8 μs, with the first few microseconds of trajectories removed for several
768 analyses to obtain data computed on equilibrated systems. All CG simulations were run in 3
769 independent replicas.

770

771 Systems for atomistic simulations were prepared with CHARMM-GUI applying CHARMM36m
772 parameters with the corresponding modified TIP3P⁹⁸. The model membranes mimicking the lipid
773 composition of the mitochondrial inner membrane (~17% CL or MLCL, 44% POPC, and 39%
774 POPE) were utilized in AA MD simulations and described previously²⁶. System size was ~20 nm
775 x 20 nm x 20 nm and included over 600,000 particles. After minimization and equilibration to 303
776 K and 1 atm, production simulations were run using standard parameters as provided by
777 CHARMM-GUI (standard semi-isotropic Berendsen barostat for equilibration while progressively
778 releasing positional restraints on the protein and standard Parrinello-Rahman semi-isotropic
779 barostat with a Nose-Hoover thermostat without restraints). PME electrostatics and a force-switch
780 cut-off of 1 nm was applied, and an integration timestep of 2 fs was used during production for
781 around 1 μ s. Analyses were performed on the second half of the production phase to probe the
782 equilibrated systems, a crucial step due to the slow convergence of lipid diffusion in AA MD
783 simulations. All AA simulations were run in 3 independent replicas.

784
785 For all our CG and AA MD simulations, we used a total charge of -2 in the polar head of both CL
786 and MLCL and utilized the corresponding parameters from MARTINI2.2p and CHARMM force
787 fields as required. In CG MD simulations, where some 10-12 atoms are grouped and the exact
788 degree of unsaturation is not resolved, only the CL(18:1)₄ was used in simulations. The AA MD
789 simulations were performed in the presence of both CL(18:1)₄ and CL(18:2)₄, and the production
790 phase of each lipid composition and replicate was assessed separately. The pKa values for
791 protein Lys and Arg sidechains were analyzed by PROPKA and predicted to be all in their charged
792 forms, and were modeled accordingly. MD trajectories were visually inspected in VMD⁹² and
793 analyzed with freely available tools and packages, detailed as follows. Atom-atom and bead-bead
794 contacts were computed with tools from the PDB manipulation suite
795 (<https://lucianoabriata.altervista.org/pdbms/>), applying 4 \AA cutoffs on non-hydrogen atoms in
796 atomistic simulations and 8 \AA cutoffs for beads in CG simulations. Minimal distances between
797 proteins and membranes were also measured with tools from the PDB manipulation suite.
798 Residue-wise residence times per lipid were computed with the PyLipID package⁹⁹ using standard
799 settings. Volumes describing atom or bead densities were computed and visualized in VMD using
800 the VolMap plugin, considering all non-hydrogen atoms when analyzing AA simulations and all
801 beads when analyzing CG simulations. Membrane deformation was computed with the
802 MembraneCurvature plugin for MDAnalysis, with standard settings and x,y grids of 14x14 tiles for
803 tetramers 1 and 3 and 18x18 tiles for tetramers 2 and 4, which required a larger membrane
804 surface. The trajectories subject to membrane deformation analysis were processed with

805 Gromacs' trjconv command, which centers the protein in the membrane by wrapping the frames
806 and removes any translation and rotation on the plane.

807

808 **Statistical Analysis**

809 Liposome co-sedimentation assays were performed in triplicate; the supernatant and pellet of
810 each replicate were run on an SDS-PAGE gel, and the relative amount of protein was quantified
811 via ImageJ. These values were converted to percentages, and only the pellet values were used
812 for statistical analysis. An unpaired two-tailed Welch's t-test was performed to compare the
813 binding of protein across various experiments. Reconstitution assays were also performed in
814 triplicate, and each replicate was quantified independently. Statistical analysis using unpaired
815 two-tailed Welch's test was carried out to compare cardiolipin with other lipids, as well as S-OPA1
816 WT and mutants. For both assays, p values <0.05 were considered statistically significant.

817

818 **Acknowledgments**

819 The authors gratefully acknowledge NYU Langone Microscopy Laboratory (RRID: SCR_017934),
820 especially Dr. Feng-Xia (Alice) Liang and Joseph Sall, for their support and assistance in this
821 work. This shared resource is partially supported by the Cancer Center Support Grant
822 P30CA016087 to the Laura and Isaac Perlmutter Cancer Center at NYU Langone Health. We
823 would also like to thank Garry Morgan and Sarah Zimmermann at the EM Services Core Facility
824 of the University of Colorado Boulder for electron microscopy training and support; the Shared
825 Instrument Pool (SIP) core facility (RRID: SCR_018986) of the Department of Biochemistry at the
826 University of Colorado Boulder for the use of the shared research instrumentation infrastructure;
827 Dr. Annette Erbse for assistance with biophysical instruments and support; Lucero Castorena
828 Casillas for carefully reading and editing the manuscript; Dr. Eric May for sharing files for MD
829 simulation analysis.

830

831 **Funding**

832 This work was supported in part by Barth Syndrome Foundation Idea Award (H.A.), a National
833 Institutes of Health grant R35 GM150942 (H.A.), Boettcher Foundation Webb-Waring Biomedical
834 Research Award (H.A.), American Heart Association Postdoctoral Fellowship 23POST1020756
835 (K.E.Z.), a National Institutes of Health grant R01 GM127673 (A.F.), a Faculty Scholar Grant from
836 the HHMI (A.F.). A.F. is an alumni investigator of the Chan Zuckerberg Biohub. LAA and MDP
837 acknowledge the Swiss National Science Foundation (SNSF) for support and the Swiss National
838 Supercomputing Centre (CSCS) for HPC resources, Switzerland.

839

840 **Author Contributions**

841 S.T., K.E.Z., A.G.I., and G.M.S. performed cloning, mutagenesis, biochemical and biophysical
842 characterizations, and carried out electron microscopy imaging and image analysis. F.R.M.
843 synthesized brominated cardiolipin for cryoEM experiments and assisted with data collection.
844 S.T., K.E.Z., G.M.S., and F.R.M. prepared liposomes for both biochemical and biophysical
845 experiments. H.A. determined the cryoEM structures, and H.A. and K.E.Z. conducted model
846 building, refinement, and validation of the cryoEM structures. L.A.A., F.T.P.M., and M.D.P.
847 performed and analyzed the molecular dynamics simulations. All authors analyzed the data,
848 discussed the results, and wrote the manuscript.

849

850 **Competing Interest Statement**

851 A.F. and F.R.M. are shareholders and employees of Altos Labs.

852 **References**

853

854 1. van Bergeijk, P., Hoogenraad, C. C. & Kapitein, L. C. Right Time, Right Place: Probing the
855 Functions of Organelle Positioning. *Trends in Cell Biology* **26**, 121–134 (2016).

856 2. Giacomello, M., Pyakurel, A., Glytsou, C. & Scorrano, L. The cell biology of mitochondrial
857 membrane dynamics. *Nat Rev Mol Cell Biol* **21**, 204–224 (2020).

858 3. Iovine, J. C., Claypool, S. M. & Alder, N. N. Mitochondrial compartmentalization: emerging
859 themes in structure and function. *Trends in Biochemical Sciences* **46**, 902–917 (2021).

860 4. Pfanner, N., Warscheid, B. & Wiedemann, N. Mitochondrial proteins: from biogenesis to
861 functional networks. *Nat Rev Mol Cell Biol* **20**, 267–284 (2019).

862 5. Monzel, A. S., Enríquez, J. A. & Picard, M. Multifaceted mitochondria: moving mitochondrial
863 science beyond function and dysfunction. *Nat Metab* **5**, 546–562 (2023).

864 6. Eisner, V., Picard, M. & Hajnoczky, G. Mitochondrial dynamics in adaptive and maladaptive
865 cellular stress responses. *Nat Cell Biol* **20**, 755–765 (2018).

866 7. Liu, A. *et al.* Fatty acyl-coenzyme A activates mitochondrial division through oligomerization
867 of MiD49 and MiD51. *Nat Cell Biol* 1–14 (2024).

868 8. Kalia, R. *et al.* Structural basis of mitochondrial receptor binding and constriction by DRP1.
869 *Nature* **558**, 401–405 (2018).

870 9. Cao, Y.-L. *et al.* MFN1 structures reveal nucleotide-triggered dimerization critical for
871 mitochondrial fusion. *Nature* **542**, 372–376 (2017).

872 10. von der Malsburg, A. *et al.* Structural mechanism of mitochondrial membrane remodelling
873 by human OPA1. *Nature* **620**, 1101–1108 (2023).

874 11. Nyenhuis, S. B. *et al.* OPA1 helical structures give perspective to mitochondrial dysfunction.
875 *Nature* **620**, 1109–1116 (2023).

876 12. Archer, S. L. Mitochondrial Dynamics — Mitochondrial Fission and Fusion in Human
877 Diseases. *N Engl J Med* **369**, 2236–2251 (2013).

878 13. Comte, J., Maisterrena, B. & Gautheron, D. C. Lipid composition and protein profiles of outer
879 and inner membranes from pig heart mitochondria. Comparison with microsomes.
880 *Biochimica et Biophysica Acta (BBA) - Biomembranes* **419**, 271–284 (1976).

881 14. Horvath, S. E. & Daum, G. Lipids of mitochondria. *Progress in Lipid Research* **52**, 590–614
882 (2013).

883 15. Ahmadpour, S. T., Mahéo, K., Servais, S., Brisson, L. & Dumas, J.-F. Cardiolipin, the
884 Mitochondrial Signature Lipid: Implication in Cancer. *IJMS* **21**, 8031 (2020).

885 16. Schlame, M. Cardiolipin remodeling and the function of tafazzin. *Biochimica et Biophysica*
886 *Acta (BBA) - Molecular and Cell Biology of Lipids* **1831**, 582–588 (2013).

887 17. Mårtensson, C. U., Doan, K. N. & Becker, T. Effects of lipids on mitochondrial functions.
888 *Biochimica et Biophysica Acta (BBA) - Molecular and Cell Biology of Lipids* **1862**, 102–113
889 (2017).

890 18. Zinser, E. *et al.* Phospholipid synthesis and lipid composition of subcellular membranes in
891 the unicellular eukaryote *Saccharomyces cerevisiae*. *J Bacteriol* **173**, 2026–2034 (1991).

892 19. Mayr, J. A. Lipid metabolism in mitochondrial membranes. *J Inherit Metab Dis* **38**, 137–144
893 (2015).

894 20. Ban, T., Heymann, J. A. W., Song, Z., Hinshaw, J. E. & Chan, D. C. OPA1 disease alleles
895 causing dominant optic atrophy have defects in cardiolipin-stimulated GTP hydrolysis and
896 membrane tubulation. *Human Molecular Genetics* **19**, 2113–2122 (2010).

897 21. Schlame, M. & Ren, M. The role of cardiolipin in the structural organization of mitochondrial
898 membranes. *Biochimica et Biophysica Acta (BBA) - Biomembranes* **1788**, 2080–2083
899 (2009).

900 22. Bustillo-Zabalbeitia, I. *et al.* Specific interaction with cardiolipin triggers functional activation
901 of Dynamin-Related Protein 1. *PLoS One* **9**, e102738 (2014).

902 23. Duncan, A. L., Robinson, A. J. & Walker, J. E. Cardiolipin binds selectively but transiently to
903 conserved lysine residues in the rotor of metazoan ATP synthases. *Proc. Natl. Acad. Sci.
904 U.S.A.* **113**, 8687–8692 (2016).

905 24. Jussupow, A., Di Luca, A. & Kaila, V. R. I. How cardiolipin modulates the dynamics of
906 respiratory complex I. *Sci. Adv.* **5**, eaav1850 (2019).

907 25. Bennett, J. A., Steward, L. R., Rudolph, J., Voss, A. P. & Aydin, H. The structure of the
908 human LACTB filament reveals the mechanisms of assembly and membrane binding. *PLoS
909 Biol* **20**, e3001899 (2022).

910 26. Manicki, M. *et al.* Structure and functionality of a multimeric human COQ7:COQ9 complex.
911 *Mol Cell* **82**, 4307–4323 e10 (2022).

912 27. Zhu, S. *et al.* Cardiolipin Remodeling Defects Impair Mitochondrial Architecture and Function
913 in a Murine Model of Barth Syndrome Cardiomyopathy. *Circ: Heart Failure* **14**, e008289
914 (2021).

915 28. Phan, K. *et al.* Uncovering pathophysiological changes in frontotemporal dementia using
916 serum lipids. *Sci Rep* **10**, 3640 (2020).

917 29. Monteiro-Cardoso, V. F. *et al.* Cardiolipin profile changes are associated to the early synaptic
918 mitochondrial dysfunction in Alzheimer's disease. *J Alzheimers Dis* **43**, 1375–1392 (2015).

919 30. Chaves-Filho, A. B. *et al.* Alterations in lipid metabolism of spinal cord linked to amyotrophic
920 lateral sclerosis. *Sci Rep* **9**, 11642 (2019).

921 31. Barth, P. G. *et al.* An X-linked mitochondrial disease affecting cardiac muscle, skeletal
922 muscle and neutrophil leucocytes. *J Neurol Sci* **62**, 327–55 (1983).

923 32. Adès, L. C. *et al.* Barth syndrome: Clinical features and confirmation of gene localisation to
924 distal Xq28. *American Journal of Medical Genetics* **45**, 327–334 (1993).

925 33. Barth, P. G. *et al.* X-linked cardioskeletal myopathy and neutropenia (Barth syndrome):
926 Respiratory-chain abnormalities in cultured fibroblasts. *Journal of Inherited Metabolic
927 Disease* **19**, 157–160 (1996).

928 34. Gedeon, A. K., Wilson, M. J., Colley, A. C., Sillence, D. O. & Mulley, J. C. X linked fatal
929 infantile cardiomyopathy maps to Xq28 and is possibly allelic to Barth syndrome. *Journal of
930 Medical Genetics* **32**, 383–388 (1995).

931 35. Abe, M. *et al.* Mechanism for Remodeling of the Acyl Chain Composition of Cardiolipin
932 Catalyzed by *Saccharomyces cerevisiae* Tafazzin. *Journal of Biological Chemistry* **291**,
933 15491–15502 (2016).

934 36. Sakamoto, O., Kitoh, T., Ohura, T., Ohya, N. & Iinuma, K. Novel missense mutation (R94S)
935 in the TAZ (G4.5) gene in a Japanese patient with Barth syndrome. *J Hum Genet* **47**, 229–
936 231 (2002).

937 37. Vesel, S. *et al.* A novel mutation in the G4.5 (TAZ) gene in kindred with Barth syndrome. *Eur
938 J Hum Genet* **11**, 97–101 (2003).

939 38. Schlame, M. *et al.* Deficiency of tetralinoleoyl-cardiolipin in Barth syndrome. *Annals of
940 Neurology* **51**, 634–637 (2002).

941 39. Claypool, S. M., McCaffery, J. M. & Koehler, C. M. Mitochondrial mislocalization and altered
942 assembly of a cluster of Barth syndrome mutant tafazzins. *J Cell Biol* **174**, 379–90 (2006).

943 40. Ikon, N. & Ryan, R. O. Cardiolipin and mitochondrial cristae organization. *Biochim Biophys
944 Acta Biomembr* **1859**, 1156–1163 (2017).

945 41. Kameoka, S., Adachi, Y., Okamoto, K., Iijima, M. & Sesaki, H. Phosphatidic Acid and
946 Cardiolipin Coordinate Mitochondrial Dynamics. *Trends in Cell Biology* **28**, 67–76 (2018).

947 42. Olichon, A. *et al.* Loss of OPA1 perturbs the mitochondrial inner membrane structure and
948 integrity, leading to cytochrome c release and apoptosis. *J Biol Chem* **278**, 7743–6 (2003).

949 43. Griparic, L., van der Wel, N. N., Orozco, I. J., Peters, P. J. & van der Bliek, A. M. Loss of the
950 intermembrane space protein Mgm1/OPA1 induces swelling and localized constrictions
951 along the lengths of mitochondria. *J Biol Chem* **279**, 18792–18798 (2004).

952 44. Cipolat, S., de Brito, O. M., Dal Zilio, B. & Scorrano, L. OPA1 requires mitofusin 1 to promote
953 mitochondrial fusion. *Proc. Natl. Acad. Sci. U.S.A.* **101**, 15927–15932 (2004).

954 45. Cogliati, S. *et al.* Mitochondrial Cristae Shape Determines Respiratory Chain
955 Supercomplexes Assembly and Respiratory Efficiency. *Cell* **155**, 160–171 (2013).

956 46. Fry, M. Y. *et al.* In situ architecture of Opa1-dependent mitochondrial cristae remodeling.
957 *The EMBO Journal* **43**, 391–413 (2024).

958 47. Del Dotto, V. *et al.* OPA1 Isoforms in the Hierarchical Organization of Mitochondrial
959 Functions. *Cell Reports* **19**, 2557–2571 (2017).

960 48. Mishra, P., Carelli, V., Manfredi, G. & Chan, D. C. Proteolytic cleavage of Opa1 stimulates
961 mitochondrial inner membrane fusion and couples fusion to oxidative phosphorylation. *Cell*
962 *Metab* **19**, 630–41 (2014).

963 49. Anand, R. *et al.* The i-AAA protease YME1L and OMA1 cleave OPA1 to balance
964 mitochondrial fusion and fission. *Journal of Cell Biology* **204**, 919–929 (2014).

965 50. Ban, T. *et al.* Molecular basis of selective mitochondrial fusion by heterotypic action between
966 OPA1 and cardiolipin. *Nat Cell Biol* **19**, 856–863 (2017).

967 51. Ge, Y. *et al.* Two forms of Opa1 cooperate to complete fusion of the mitochondrial inner-
968 membrane. *eLife* **9**, e50973 (2020).

969 52. Zhang, D. *et al.* Cryo-EM structures of S-OPA1 reveal its interactions with membrane and
970 changes upon nucleotide binding. *eLife* **9**, e50294 (2020).

971 53. Jimah, J. R. & Hinshaw, J. E. Structural Insights into the Mechanism of Dynamin Superfamily
972 Proteins. *Trends in Cell Biology* **29**, 257–273 (2019).

973 54. Moss, F. R. *et al.* Brominated lipid probes expose structural asymmetries in constricted
974 membranes. *Nat Struct Mol Biol* **30**, 167–175 (2023).

975 55. Arnold, W. R. *et al.* Structural basis of TRPV1 modulation by endogenous bioactive lipids.
976 *Nat Struct Mol Biol* 1–9 (2024) doi:10.1038/s41594-024-01299-2.

977 56. Kimanis, D., Dong, L., Sharov, G., Nakane, T. & Scheres, S. H. W. New tools for automated
978 cryo-EM single-particle analysis in RELION-4.0. *Biochem J* **478**, 4169–4185 (2021).

979 57. Cullis, P. R., Verkleij, A. J. & Ververgaert, P. H. J. Th. Polymorphic phase behaviour of
980 cardiolipin as detected by ³¹P NMR and freeze-fracture techniques. Effects of calcium,
981 dibucaine and chlorpromazine. *Biochimica et Biophysica Acta (BBA) - Biomembranes* **513**,
982 11–20 (1978).

983 58. Vasilenko, I., De Kruijff, B. & Verkleij, A. J. Polymorphic phase behaviour of cardiolipin from
984 bovine heart and from *Bacillus subtilis* as detected by ³¹P-NMR and freeze-fracture

985 techniques. Effects of Ca²⁺, Mg²⁺, Ba²⁺ and temperature. *Biochim Biophys Acta* **684**, 282–
986 286 (1982).

987 59. Ortiz, A., Killian, J. A., Verkleij, A. J. & Wilschut, J. Membrane Fusion and the Lamellar-to-
988 Inverted-Hexagonal Phase Transition in Cardiolipin Vesicle Systems Induced by Divalent
989 Cations. *Biophysical Journal* **77**, 2003–2014 (1999).

990 60. Casares, D., Escribá, P. V. & Rosselló, C. A. Membrane Lipid Composition: Effect on
991 Membrane and Organelle Structure, Function and Compartmentalization and Therapeutic
992 Avenues. *Int J Mol Sci* **20**, 2167 (2019).

993 61. Van Meer, G., Voelker, D. R. & Feigenson, G. W. Membrane lipids: where they are and how
994 they behave. *Nat Rev Mol Cell Biol* **9**, 112–124 (2008).

995 62. Chen, J., Shao, J., Wang, Y., Wu, K. & Huang, M. OPA1, a molecular regulator of dilated
996 cardiomyopathy. *J Cellular Molecular Medi* **27**, 3017–3025 (2023).

997 63. Yang, L. *et al.* OPA1-Exon4b Binds to mtDNA D-Loop for Transcriptional and Metabolic
998 Modulation, Independent of Mitochondrial Fusion. *Front. Cell Dev. Biol.* **8**, 180 (2020).

999 64. Schlame, M., Rua, D. & Greenberg, M. L. The biosynthesis and functional role of cardiolipin.
1000 *Prog Lipid Res* **39**, 257–288 (2000).

1001 65. Rand, R. P. & Sengupta, S. Cardiolipin forms hexagonal structures with divalent cations.
1002 *Biochim Biophys Acta* **255**, 484–492 (1972).

1003 66. De Kruijff, B. *et al.* Further aspects of the Ca²⁺-dependent polymorphism of bovine heart
1004 cardiolipin. *Biochimica et Biophysica Acta (BBA) - Biomembranes* **693**, 1–12 (1982).

1005 67. East, J. M. & Lee, A. G. Lipid selectivity of the calcium and magnesium ion dependent
1006 adenosinetriphosphatase, studied with fluorescence quenching by a brominated
1007 phospholipid. *Biochemistry* **21**, 4144–51 (1982).

1008 68. Hristova, K. & White, S. H. Determination of the hydrocarbon core structure of fluid
1009 dioleoylphosphocholine (DOPC) bilayers by x-ray diffraction using specific bromination of
1010 the double-bonds: effect of hydration. *Biophys J* **74**, 2419–33 (1998).

1011 69. Persson, D. *et al.* Vesicle size-dependent translocation of penetratin analogs across lipid
1012 membranes. *Biochimica et Biophysica Acta (BBA) - Biomembranes* **1665**, 142–155 (2004).

1013 70. Glytsou, C. *et al.* Optic Atrophy 1 Is Epistatic to the Core MICOS Component MIC60 in
1014 Mitochondrial Cristae Shape Control. *Cell Reports* **17**, 3024–3034 (2016).

1015 71. Cipolat, S. *et al.* Mitochondrial Rhomboid PARL Regulates Cytochrome c Release during
1016 Apoptosis via OPA1-Dependent Cristae Remodeling. *Cell* **126**, 163–175 (2006).

1017 72. Ban, T., Heymann, J. A. W., Song, Z., Hinshaw, J. E. & Chan, D. C. OPA1 disease alleles
1018 causing dominant optic atrophy have defects in cardiolipin-stimulated GTP hydrolysis and
1019 membrane tubulation. *Hum Mol Genet* **19**, 2113–2122 (2010).

1020 73. Ban, T. *et al.* Prohibitin 1 tethers lipid membranes and regulates OPA1-mediated membrane
1021 fusion. *J Biol Chem* **301**, 108076 (2025).

1022 74. Gripasic, L., Kanazawa, T. & Van Der Bliek, A. M. Regulation of the mitochondrial dynamin-
1023 like protein Opa1 by proteolytic cleavage. *The Journal of Cell Biology* **178**, 757–764 (2007).

1024 75. Song, Z., Chen, H., Fiket, M., Alexander, C. & Chan, D. C. OPA1 processing controls
1025 mitochondrial fusion and is regulated by mRNA splicing, membrane potential, and Yme1L.
1026 *The Journal of Cell Biology* **178**, 749–755 (2007).

1027 76. Tondera, D. *et al.* SLP-2 is required for stress-induced mitochondrial hyperfusion. *EMBO J*
1028 **28**, 1589–1600 (2009).

1029 77. Duncan, A. L. Monolysocardiolipin (MLCL) interactions with mitochondrial membrane
1030 proteins. *Biochemical Society Transactions* **48**, 993–1004 (2020).

1031 78. Powell, G. L. & Marsh, D. Polymorphic phase behavior of cardiolipin derivatives studied by
1032 phosphorus-31 NMR and x-ray diffraction. *Biochemistry* **24**, 2902–2908 (1985).

1033 79. Boyd, K. J., Alder, N. N. & May, E. R. Molecular Dynamics Analysis of Cardiolipin and
1034 Monolysocardiolipin on Bilayer Properties. *Biophysical Journal* **114**, 2116–2127 (2018).

1035 80. Wilson, B. A., Ramanathan, A. & Lopez, C. F. Cardiolipin-Dependent Properties of Model
1036 Mitochondrial Membranes from Molecular Simulations. *Biophysical Journal* **117**, 429–444
1037 (2019).

1038 81. Venkatraman, K., Lee, C. T. & Budin, I. Setting the curve: the biophysical properties of lipids
1039 in mitochondrial form and function. *Journal of Lipid Research* **65**, 100643 (2024).

1040 82. Ardail, D. *et al.* Mitochondrial contact sites. Lipid composition and dynamics. *Journal of*
1041 *Biological Chemistry* **265**, 18797–18802 (1990).

1042 83. Schindelin, J. *et al.* Fiji: an open-source platform for biological-image analysis. *Nat Methods*
1043 **9**, 676–82 (2012).

1044 84. Mastronarde, D. N. Automated electron microscope tomography using robust prediction of
1045 specimen movements. *J Struct Biol* **152**, 36–51 (2005).

1046 85. Rohou, A. & Grigorieff, N. CTFFIND4: Fast and accurate defocus estimation from electron
1047 micrographs. *Journal of Structural Biology* **192**, 216–221 (2015).

1048 86. Pettersen, E. F. *et al.* UCSF Chimera--a visualization system for exploratory research and
1049 analysis. *J Comput Chem* **25**, 1605–12 (2004).

1050 87. Kucukelbir, A., Sigworth, F. J. & Tagare, H. D. Quantifying the local resolution of cryo-EM
1051 density maps. *Nat Methods* **11**, 63–5 (2014).

1052 88. Morin, A. *et al.* Collaboration gets the most out of software. *Elife* **2**, e01456 (2013).

1053 89. Liebschner, D. *et al.* Macromolecular structure determination using X-rays, neutrons and
1054 electrons: recent developments in *Phenix*. *Acta Crystallogr D Struct Biol* **75**, 861–877 (2019).

1055 90. Emsley, P., Lohkamp, B., Scott, W. G. & Cowtan, K. Features and development of Coot.
1056 *Acta Crystallogr D Biol Crystallogr* **66**, 486–501 (2010).

1057 91. Williams, C. J. *et al.* MolProbity: More and better reference data for improved all-atom
1058 structure validation. *Protein Science* **27**, 293–315 (2018).

1059 92. Humphrey, W., Dalke, A. & Schulten, K. VMD: visual molecular dynamics. *J Mol Graph* **14**,
1060 33–8, 27–8 (1996).

1061 93. Jo, S., Kim, T., Iyer, V. G. & Im, W. CHARMM-GUI: a web-based graphical user interface for
1062 CHARMM. *J Comput Chem* **29**, 1859–65 (2008).

1063 94. Bauer, P., Hess, B. & Lindahl, E. Gromacs 2022 Manual. (2022).

1064 95. de Jong, D. H. *et al.* Improved Parameters for the Martini Coarse-Grained Protein Force
1065 Field. *J Chem Theory Comput* **9**, 687–97 (2013).

1066 96. Periole, X., Cavalli, M., Marrink, S. J. & Ceruso, M. A. Combining an Elastic Network with a
1067 Coarse-Grained Molecular Force Field: Structure, Dynamics, and Intermolecular
1068 Recognition. *J Chem Theory Comput* **5**, 2531–43 (2009).

1069 97. Qi, Y. *et al.* CHARMM-GUI Martini Maker for Coarse-Grained Simulations with the Martini
1070 Force Field. *J Chem Theory Comput* **11**, 4486–94 (2015).

1071 98. Huang, J. *et al.* CHARMM36m: an improved force field for folded and intrinsically disordered
1072 proteins. *Nat Methods* **14**, 71–73 (2017).

1073 99. Song, W. *et al.* PyLipID: A Python Package for Analysis of Protein-Lipid Interactions from
1074 Molecular Dynamics Simulations. *J Chem Theory Comput* **18**, 1188–1201 (2022).

1075

1076 **Figure Legends**

1077 **Figure 1. Interactions between lipids and S-OPA1 residues and changes in membrane**
1078 **topology.** **(a)** The S-OPA1 tetramer model was extracted from the cryoEM structure of the membrane-bound S-OPA1 polymer in membrane-proximal conformation (PDB ID: 8CT1) and fitted into the cryoEM density map (EMDB ID: 26977). Each subunit of the tetramer is shown in surface representation and a different color, matching those in panel (c). IL, Inner Leaflet; OL, Outer Leaflet; PL, Protein Layer. **(b)** Structural organization of human S-OPA1. The primary sequence of S-OPA1 contains four domains: bundle signaling element (BSE), GTPase, stalk, and paddle. The extracted ribbon model for S-OPA1 monomer is colored in orange (GTPase), red (BSE), blue (stalk), and green (PD) to highlight the domain organization of S-OPA1, and the surface is depicted as semi-transparent solid density. This color scheme is used throughout the manuscript, except otherwise noted. **(c)** Tetramer 1 after docking onto a membrane containing 17% CL, 44% POPC, and 39% POPE via unbiased CG MD simulations. Each OPA1 subunit is shown in surface representation with the colors defined in **(a)**. Note the curvature experienced by the membrane in the direction of tubulation with OPA1 remaining outside, quantified in panel **h**. The average densities for all beads that make up the CG MD simulation lipids are shown in magenta (CL), green (POPC), and cyan (POPE). Despite being minoritarian in composition, the CL molecules cluster very strongly at the protein-membrane contact sites. Bottom view of the S-OPA1 tetramer simulated on CL-enriched membranes is shown on the right. **(d)** Residence times for contacts between protein and lipid beads are shown for CL, POPE, and POPC and are calculated for all four subunits in each of the three CG MD simulation replicates for tetramer 1. The inset above the plot for CL shows an OPA1 tetramer in surface representation with the residence times mapped as shades increasing from grey to red, to highlight the positions of those residues with longer residence times. **(e)** The average number of protein-lipid contacts per residue was calculated using the last 300 ns of the AA MD simulations in 3 independent replicas. **(f)** CL density averaged from AA MD simulations also shows that this lipid clusters strongly at OPA1-membrane contact sites, especially around the MIL (residues 771 to 781) and the docking region (residues 857 to 861). The simulations were set up by using a monomeric S-OPA1 model extracted from tetramer 1 and placing it onto membranes with the same lipid composition, as in the CG simulations; however, CL(18:2)₄ was used for AA MD simulations as this is the main CL species in both cardiac and skeletal muscle tissues. **(g)** The heat map was generated using one of the replicas that shows strong binding to the membrane and displays the number of membrane contacts for S-OPA1 residues over time (nanoseconds). For more details about CG and AA MD simulations, please see Methods. **(h)** Membrane deformation analysis in CG MD simulations.

1110 Membrane bending activity of the S-OPA1 tetramer 1 measured in CG MD simulations with a
1111 membrane patch containing 44% POPC, 39% POPE, and 17% CL or POPS. The three graphs
1112 correspond to top views of the membranes, color-coded by the replica- and trajectory-averaged
1113 (last 4 μ s out of 8 μ s) deformations along the membrane normal, measured in 1/ \AA . The images
1114 (from left to right) show the CL membrane without protein, the CL membrane with S-OPA1
1115 tetramer, and the POPS membrane with S-OPA1 tetramer. Red and blue colors indicate
1116 membrane pulling and pushing in the direction of the membrane normal, respectively. The
1117 comparison of the three different membrane deformation analyses indicate that the S-OPA1
1118 tetramer was able to bend membranes containing both CL and POPS, but the extent of
1119 deformation is decreased in the presence of POPS (fewer areas of deep blue and deep red). The
1120 membrane pulling in POPS-containing membranes peaks at $\sim 0.3 \text{ \AA}^{-1}$, while membrane pushing
1121 only reaches to -0.2 \AA^{-1} in one region and is even weaker in others. The dashed lines correspond
1122 to an overlay of the position of the OPA1 tetramer.
1123

1124 **Figure 2. Membrane binding and remodeling experiments with different CL Species** **(a)** Co-
1125 sedimentation assays of S-OPA1 WT were performed using liposomes containing five different
1126 CL species: CL(16:0)₄, CL(18:0)₄, CL(18:1)₄, CL(16:0)₂-(18:1)₂, and CL(18:2)₄. All liposomes
1127 share a common composition of 45% POPC, 22% POPE, and 8% L-PI, with the remaining 25%
1128 composed of the respective CL species. Supernatant and pellet samples were collected after
1129 centrifugation, subjected to SDS-PAGE, and quantified using ImageJ. S, supernatant. P, pellet.
1130 **(b)** The assays were performed in triplicate, and the binding activity was quantified from the pellet
1131 fractions. Statistical significance was assessed using a two-tailed unpaired Welch's t-test based
1132 on $n=3$ independent experiments comparing binding across various CL-containing liposome
1133 compositions. P -values are represented on the graph, and $p<0.05$ is considered to be statistically
1134 significant. **(c)** Remodeled area (μm^2) was calculated by measuring the surface area of membrane
1135 tubules. Each lipid composition was tested in three independent reconstitution assays, and
1136 negative-stain TEM imaging was performed on each replicate. The total remodeled area was
1137 calculated per micrograph and a total of 75 negative stain micrographs were analyzed per lipid
1138 composition. **(d)** S-OPA1 filaments were counted in each micrograph and plotted against the
1139 corresponding lipid composition. **(c, d)** Error bars represent the standard error of the mean
1140 (s.e.m.). Statistical significance was assessed using a two-tailed unpaired Welch's t-test with $n=3$
1141 independent experiments. P -values are annotated on the graph, and $p<0.05$ is considered
1142 statistically significant. **(e)** Quantification of filament morphology per liposome composition. Each
1143 remodeled filament was counted and assigned to one of the three classes: large (cyan), medium

1144 (purple), or small (pink). Filament sizes were defined as small at 0-0.01 μm^2 , medium for 0.01-
1145 0.05 μm^2 , and large if >0.05 μm^2 . The percentage of each class is calculated per liposome
1146 composition and is shown as a stacked bar graph.

1147

1148 **Figure 3. Characterization of key membrane interface residues.** (a) The SDS-PAGE analysis
1149 of the co-sedimentation assays with S-OPA1 WT, MIL, R858A, and MIL-R858 double-mutant in
1150 the presence and absence of CL-containing liposomes. S, supernatant. P, pellet. A lipid mixture
1151 of 45% POPC, 22% POPE, 8% L-PI, and 25% CL(18:2)₄ was used to prepare liposomes. (b)
1152 Supernatant and pellet samples were collected after centrifugation, subjected to SDS-PAGE, and
1153 quantified using ImageJ. The assays were performed in triplicate, and the binding activity was
1154 quantified from the pellet fractions. Statistical significance was assessed using a two-tailed
1155 unpaired Welch's t-test based on $n=3$ independent experiments comparing S-OPA1 WT to mutant
1156 constructs. P -values are represented on the graph, and $p<0.05$ is considered to be statistically
1157 significant. (c) The reconstitution assays for WT and mutant S-OPA1 samples were visualized by
1158 negative-stain TEM. Scale bar is 100 nm. (d) Remodeled area (μm^2) was calculated by measuring
1159 the surface area of membrane tubules. WT and mutant samples were tested in three independent
1160 reconstitution assays, and negative stain TEM imaging was performed on each replicate. The
1161 total tubulated area was calculated in each micrograph and a total of 75 micrographs were
1162 analyzed per sample. (e) S-OPA1 filaments per micrograph were counted and plotted against the
1163 corresponding sample. (d, e) Error bars represent the standard error of the mean (s.e.m.).
1164 Statistical significance was assessed using a two-tailed unpaired Welch's t-test with $n=3$
1165 independent experiments. P -values are annotated on the graph, and $p<0.05$ is considered
1166 statistically significant. (f) Quantification of filament morphology per liposome composition. Each
1167 remodeled filament was counted and assigned to one of the three classes: large, medium, or
1168 small. Filament sizes were defined as small at 0-0.01 μm^2 (pink), medium for 0.01-0.05 μm^2
1169 (purple), and large if >0.05 μm^2 (cyan). The percentage of each class is calculated per sample
1170 and is shown as a stacked bar graph.

1171

1172 **Figure 4. CryoEM reconstruction of human S-OPA1 bound to CL-Br-enriched membranes.**
1173 (a) Structure of tetrabrominated CL. (b) The side view for surface representation and the
1174 corresponding ribbon diagram of the S-OPA1 tetramer 1 oriented into the cryoEM density map.
1175 The inset window shows the close-up view of the paddle domain (green) and conserved MIL
1176 region interacting with membranes. (c) Tetrameric ribbon model of the S-OPA1 bound to CL-Br
1177 membranes. The four structural domains are colored as follows: GTPase (orange), BSE (red),

1178 Stalk (blue), and Paddle (green). **(d)** A gray-scale slice of the cryoEM 3D reconstruction of the
1179 membrane-bound S-OPA1 filament. The red rectangle indicates the position of the magnified view
1180 shown in panel E. **(e)** The difference map calculated from brominated and native protein-lipid
1181 reconstructions shows additional densities (magenta) located near the PDs (green) of S-OPA1.
1182 **(f)** Gray-scale slices of native and brominated membranes along the helical axis. The cryoEM
1183 reconstruction of S-OPA1 assembly bound to CL-Br-containing membranes shows CL
1184 enrichment in the outer leaflet. **(g)** Radial profiles from the cryoEM 3D reconstructions indicate
1185 the location of the surplus signals attributed to halogen scattering. The red box in panel A indicates
1186 the region used in intensity analysis.

1187

1188 **Figure 5. S-OPA1 interactions with MLCL-containing membranes.** **(a)** Membrane deformation
1189 calculations are shown for one of the three independent replicas using S-OPA1 tetramer 1 and
1190 model membranes containing either CL (left) or MLCL (right). Red and blue colors indicate
1191 membrane pulling and pushing in the direction of z, respectively. The membrane deformation
1192 activity of tetramer 1, particularly its ability to push down on the sides, is reduced in the presence
1193 of MLCL. **(b)** The co-sedimentation assays with S-OPA1 WT and liposomes containing CL and
1194 increasing molar ratios of MLCL. A lipid mixture of 45% POPC, 22% POPE, 8% L-PI, and 25%
1195 CL and/or MLCL was used to prepare five different liposomes. The CL:MLCL ratios used for
1196 liposome preparations as follows: 25% CL; 24% CL and 1% MLCL; 22% CL and 3% MLCL; 20%
1197 CL and 5% MLCL; and 25% MLCL. Supernatant and pellet samples from the co-sedimentation
1198 assays were harvested after centrifugation and analyzed by SDS-PAGE. **(c)** The assays were
1199 performed in triplicate and gel images were quantified by ImageJ. The binding activity of S-OPA1
1200 WT was quantified from pellet fractions, and statistical significance was assessed using a two-
1201 tailed unpaired Welch's t-test based on $n=3$ independent experiments, comparing CL-containing
1202 liposomes to those with increasing molar concentrations of MLCL. P -values are represented on
1203 the graph, and $p < 0.05$ is considered to be statistically significant. **(d)** Representative negative-
1204 stain TEM images of reconstitution assays in the presence of CL- and MLCL-containing
1205 liposomes. Increasing molar ratios of MLCL alter the membrane remodeling activity of S-OPA1.
1206 Scale bars are 100 nm. **(e)** Remodeled area (μm^2) was calculated by measuring the surface area
1207 of membrane tubules. Each lipid composition was tested in three independent reconstitution
1208 assays, and negative stain TEM imaging was performed on each replicate. The total remodeled
1209 area was calculated per micrograph and a total of 75 negative stain micrographs were analyzed
1210 per sample. **(f)** S-OPA1 filaments were counted in each micrograph and plotted against the
1211 corresponding lipid composition. **(e, f)** Error bars represent the standard error of the mean

1212 (s.e.m.). Statistical significance was assessed using a two-tailed unpaired Welch's *t*-test with $n=3$
1213 independent experiments. *P*-values are annotated on the graph, and $p<0.05$ is considered
1214 statistically significant. **(g)** Quantification of filament morphology per liposome composition. Each
1215 remodeled filament was counted and assigned to one of the three classes: large (cyan), medium
1216 (purple), or small (pink). Filament sizes were defined as small at 0-0.01 μm^2 , medium for 0.01-
1217 0.05 μm^2 , and large if $>0.05 \mu\text{m}^2$. The percentage of each class is calculated per liposome
1218 composition and is shown as a stacked bar graph.

1219

1220 **Figure 6. Proposed model of how CL controls mitochondrial remodeling.** OPA1 interactions
1221 with randomly distributed CL molecules in membranes trigger the clustering of CL near protein-
1222 membrane contact sites and facilitate the remodeling of membranes. The accumulation of MLCL
1223 in membranes restricts the membrane remodeling activity of OPA1 and causes abnormalities in
1224 mitochondrial morphology.

1225

1226 **Supplementary Figure Legends**

1227 **Supplementary Figure 1. Description of four OPA1 tetramers used in MD simulations. (a-c)**
1228 Three tetrameric subassemblies of the S-OPA1 polymer (tetramers 2, 3, and 4) were fitted into
1229 the corresponding density map, which is transparently visible. Each monomer is shown in surface
1230 representation and colored differently for clarity. Tetramer 2 **(a)** is extracted from the polymeric
1231 model in membrane-proximal conformation, while tetramers 3 **(b)** and 4 **(c)** are extracted from the
1232 polymeric model that represents the membrane-distal conformation of the S-OPA1 polymer. **(d,**
1233 **e)** Superimposition of the S-OPA1 tetramers assembled using different oligomerization interfaces.
1234 **(d)** Tetramers representing the conserved crisscross association of dynamin superfamily proteins.
1235 **(e)** The newly identified interface 7 mediates the formation of other tetrameric assemblies in the
1236 membrane-bound state. The root-mean-square deviation (RMSD) is calculated using the CLICK
1237 server.

1238

1239 **Supplementary Figure 2. An overview of the MD simulation setup. (a)** A representative image
1240 of the membrane patch used in CG MD simulations. The lipid molecules are shown in magenta
1241 (CL), green (POPC), and cyan (POPE). **(b)** The trajectories of OPA1-membrane interactions
1242 using the S-OPA1 starting model positioned $\sim 60 \text{ \AA}$ away from the membrane. The graph shows
1243 the minimal distance between the protein and membrane, calculated from five independent
1244 replicas of the simulation. **(c)** S-OPA1 tetramer binds to the membrane patch via the membrane-
1245 inserting loop (MIL) and docking regions in CG MD simulations. The subunits of the S-OPA1

1246 tetramer are colored blue, yellow, orange, and gray. The MIL region is highlighted in green. S-
1247 OPA1 tetramers are positioned close to the membrane patch in the simulations. After a <1 μ s
1248 simulation time, the tetramers rapidly formed charge-charge and hydrophobic interactions with
1249 the bilayer lipids and deformed the membrane patch. **(d)** The S-OPA1 tetramers containing
1250 mutations within the MIL and docking regions do not bind the membrane patch and remain in
1251 solution within the timescale of the simulations.

1252

1253 **Supplementary Figure 3. Comparison of residence times for CL and MLCL lipids in AA and**
1254 **CG MD simulations.** **(a)** Residence times for contacts between S-OPA1 residues and CL (blue
1255 line), MLCL (red line), and POPS (green line) lipids in CG MD simulations. The data was averaged
1256 over four subunits in each tetramer and three replicas. **(b)** Average number of protein-lipid
1257 contacts calculated from three replicas of AA MD simulations using S-OPA1 tetramer and CL-
1258 and MLCL-enriched membranes. **(c, d)** Molecular interactions between S-OPA1 and CL
1259 headgroups. Close-up views of the two CL-binding motifs highlight key protein-lipid interactions
1260 in AA MD simulations. The paddle domain of S-OPA1 is shown in green, and CL molecules are
1261 colored in light pink. The distances between S-OPA1 residues and CL molecules are shown in
1262 Angstroms.

1263

1264 **Supplementary Figure 4. Membrane deformation analysis of S-OPA1 tetramer in CG MD**
1265 **simulations.** Red and blue colors indicate membrane pulling and pushing in the direction of z,
1266 respectively. The x and y axes indicate the number of membrane tiles; each tile represents 15 \AA .
1267 **(a)** Membrane deformation calculations are shown for two other independent replicas using S-
1268 OPA1 tetramer 1 and model membranes containing either CL (left) or MLCL (right). The
1269 membrane deformation activity of tetramer 1, particularly its ability to push down on the sides, is
1270 reduced in the presence of MLCL. **(b)** Average membrane deformation was calculated for S-
1271 OPA1 tetramers 2, 3, and 4. A comparison of CL- and MLCL-containing membranes indicates
1272 reduced membrane deformation in the presence of MLCL for tetramer 3. While the CG MD
1273 simulations with tetramers 1 and 3 display significant membrane bending with CL-containing
1274 membranes, tetramers 2 and 4 show no visible difference between the two membranes.

1275

1276 **Supplementary Figure 5. Biochemical characterization of human S-OPA1 construct and**
1277 **sequence alignment of the paddle domain.** **(a)** A representative size-exclusion
1278 chromatography (SEC) profile of S-OPA1 WT and **(b)** SDS-PAGE of S-OPA1 protein following
1279 SEC. **(c)** The sequence alignment of paddle domain residues (736 to 860) demonstrates high

1280 sequence conservation across 33 species. Solid black lines below the sequence alignment
1281 indicate the boundaries of the membrane-inserting loop (MIL) and docking regions.

1282

1283 **Supplementary Figure 6. Membrane binding and remodeling experiments of S-OPA1 with**
1284 **various lipids. (a)** Co-sedimentation assays of S-OPA1 WT using six different liposomes
1285 containing POPC, POPE, POPS, POPG, L-PI, and CL at various concentrations. The
1286 PC/PE/PI/CL liposomes contain 45% POPC, 22% POPE, 8% L-PI, and 25% CL; The
1287 PC/PE/PI/PS liposomes contain 45% POPC, 22% POPE, 8% L-PI, and 25% POPS; The
1288 PC/PE/PI/PG liposomes contain 45% POPC, 22% POPE, 8% L-PI, and 25% POPG; the
1289 PC/PE/PI liposomes contain 70% POPC, 22% POPE, and 8% L-PI; the PC/PE liposomes
1290 contains 78% POPC and 22% POPE; and the PC liposomes contain 100% POPC. Supernatant
1291 and pellet samples from the co-sedimentation assays were harvested after centrifugation and
1292 analyzed by SDS-PAGE. **(b)** The assays were performed in triplicate and gel images were
1293 quantified by ImageJ. The binding activity of S-OPA1 WT was quantified from pellet fractions, and
1294 statistical significance was assessed using a two-tailed unpaired Welch's t-test based on $n=3$
1295 independent experiments, comparing CL-containing liposomes to other liposomes with various
1296 compositions. P -values are represented on the graph, and $p<0.05$ is considered to be statistically
1297 significant. **(c)** Reconstitution assays were performed with the same liposomes as in **(a)**. The
1298 samples were incubated for ~4 hours at room temperature and visualized by using negative-stain
1299 TEM. Scale bar is 100 nm. **(d)** Remodeled area (μm^2) was calculated by measuring the surface
1300 area of membrane tubules. Each lipid composition was tested in three independent reconstitution
1301 assays, and negative stain TEM imaging was performed on each replicate. The total remodeled
1302 area was calculated per micrograph, and a total of 75 negative stain micrographs were analyzed
1303 per lipid composition. **(e)** S-OPA1 filaments were counted in each micrograph and plotted against
1304 the corresponding lipid composition. **(d, e)** Error bars represent the standard error of the mean
1305 (s.e.m.). Statistical significance was assessed using a two-tailed unpaired Welch's t-test with $n=3$
1306 independent experiments. P -values are annotated on the graph, and $p<0.05$ is considered
1307 statistically significant. **(f)** Quantification of filament morphology per liposome composition. Each
1308 remodeled filament was counted and assigned to one of the three classes: large, medium, or
1309 small. Filament sizes were defined as small at 0-0.01 μm^2 (pink), medium for 0.01-0.05 μm^2
1310 (purple), and large if $>0.05 \mu\text{m}^2$ (cyan). The percentage of each class is calculated per sample
1311 and is shown as a stacked bar graph.

1312

1313 **Supplementary Figure 7. Negative-stain TEM images of liposomes and lipid nanotubes for**
1314 **different CL species. (a)** Representative negative-stain TEM images show empty liposomes and
1315 membrane tubulation in the presence of S-OPA1 WT. All liposomes share a common composition
1316 of 45% POPC, 22% POPE, and 8% L-PI, with the remaining 25% composed of five different CL
1317 species: CL(16:0)₄, CL(18:0)₄, CL(18:1)₄, CL(16:0)₂-(18:1)₂, and CL(18:2)₄. Protein samples were
1318 able to bind and remodel membranes containing CL(18:1)₄, CL(16:0)₂-(18:1)₂, and CL(18:2)₄,
1319 whereas liposomes prepared with CL(16:0)₄, and CL(18:0)₄ impaired S-OPA1's ability to bind and
1320 remodel lipid membranes. **(b)** Negative-stain TEM images of lipid nanotubes composed of five
1321 different CL species, CL(16:0)₄, CL(18:0)₄, CL(18:1)₄, CL(16:0)₂-(18:1)₂, and CL(18:2)₄, in the
1322 presence and absence of S-OPA1 WT. The nanotubes were composed of 90% Galactosyl(β)
1323 Ceramide and 10% of the respective CL species. Similar to above experiments, lipid nanotubes
1324 composed of CL(16:0)₄, and CL(18:0)₄ hindered S-OPA1-membrane interactions, while
1325 CL(18:1)₄, CL(16:0)₂-(18:1)₂, and CL(18:2)₄ nanotubes promoted the formation of S-OPA1
1326 filaments on pre-curved membranes *in vitro*. Scale bars are 100 nm.

1327
1328 **Supplementary Figure 8. Validation of brominated cardiolipin. (a)** Mass spectrum of
1329 brominated cardiolipin from 780 to 1280 mass to charge ratio (m/z). **(b)** Zoomed-in view of the
1330 mass spectrum from 1042 to 1052 m/z. **(c, d)** The brominated cardiolipin chemistry was validated
1331 by small ligand NMR. The NMR Spectrum of cardiolipin H¹ **(c)** and brominated cardiolipin H¹ **(d)**.

1332
1333 **Supplementary Figure 9. Negative-stain TEM images of various liposomes and lipid**
1334 **nanotubes. (a)** Representative negative-stain TEM images of reconstitution assays show
1335 cylindrical and spherical liposomes in the presence and absence of S-OPA1 WT. All liposomes
1336 share a common composition of 45% POPC, 22% POPE, and 8% L-PI, with the remaining 25%
1337 composed of either native or brominated CL. Protein samples bind and form higher-order
1338 assemblies on brominated and native liposomes. Different molar concentrations of CL and MLCL
1339 were used to prepare various liposomes **(b)** and lipid nanotubes **(c)**. **(b)** Liposomes were prepared
1340 with varying CL:MLCL ratios, maintaining the same base lipid composition as in **(a)**. The CL:MLCL
1341 ratios used for liposome preparations are as follows: 24% CL and 1% MLCL; 22% CL and 3%
1342 MLCL; 20% CL and 5% MLCL; and 25% MLCL. **(c)** Similarly, the lipid nanotubes were composed
1343 of 90% Galactosyl(β) Ceramide, and the remaining 10% consisted of the following CL:MLCL ratios:
1344 9% CL and 1% MLCL; 7% CL and 3% MLCL; 5% CL and 5% MLCL; and 10% MLCL. **(b, c)**
1345 Negative-stain TEM micrographs show that increasing concentrations of MLCL do not change the
1346 morphology of liposomes and lipid nanotubes compared to the CL-enriched lipid bilayers. **(d)** Lipid

1347 nanotubes prepared with low molar concentrations of MLCL do not disrupt the formation of S-
1348 OPA1 filaments on pre-curved membranes *in vitro*. Scale bars are 100 nm.

1349

1350 **Supplementary Figure 10. CryoEM imaging and image analysis of S-OPA1 assemblies**
1351 **bound to brominated liposomes.** **(a)** Electron cryo-micrograph showing S-OPA1 filaments
1352 assembled on liposomes containing CL-Br. **(b)** Representative 2D class averages of S-OPA1
1353 filament segments. **(c)** Gold-standard Fourier Shell Correlation (FSC) curve of the final density
1354 map. **(d)** Local resolution estimates for the cryoEM 3D reconstruction. Both horizontal and vertical
1355 slices through cryo-EM densities are shown. **(e)** S-OPA1 tetramer bound to brominated
1356 nanotubes (colored) superimposed with the tetrameric model bound to native nanotubes (gray)
1357 shows minimal structural differences between the two models. **(f)** A gray-scale slice of the
1358 difference map of S-OPA1 polymer bound to native and brominated liposomes shows CL
1359 enrichment in the outer leaflet. IL, Inner Leaflet; OL, Outer Leaflet; PD, Paddle Domain.

1360

1361 **Supplementary Figure 11. CryoEM data processing flowchart of S-OPA1 bound to**
1362 **brominated cardiolipin-containing membranes.** Details of cryoEM data collection and image
1363 analysis are described in the methods section.

1364

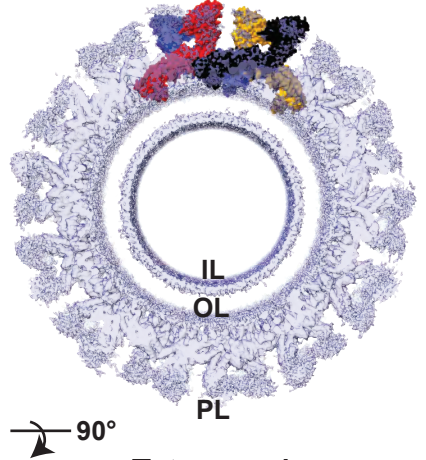
1365 **Supplementary Table 1. Cryo-EM data collection, refinement, and validation statistics for**
1366 **the two tetrameric S-OPA1 models.**

1367

1368 **Supplementary Table 2. List of liposome compositions used in reconstitution assays, co-**
1369 **sedimentation experiments, and cryoEM imaging.**

a

CryoEM density map



Tetramer 1



195 263 281

Linker BSE

GTPase Domain

561 589

BSE

736

Stalk

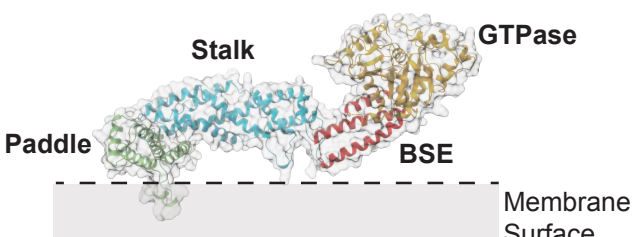
865

Paddle

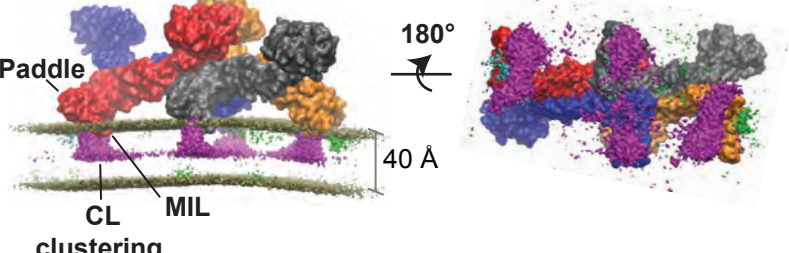
928 960

Stalk BSE

S-OPA1



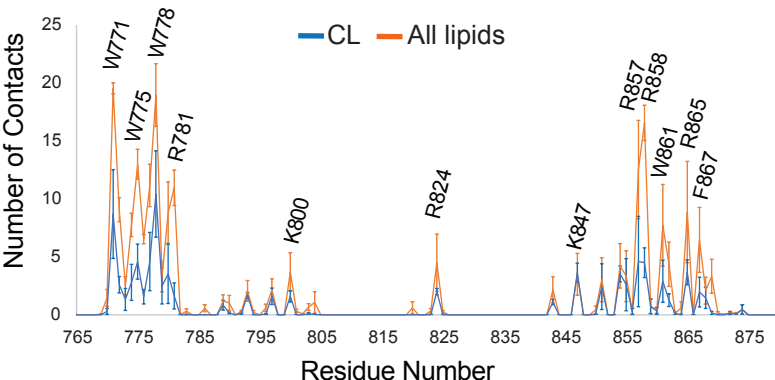
c



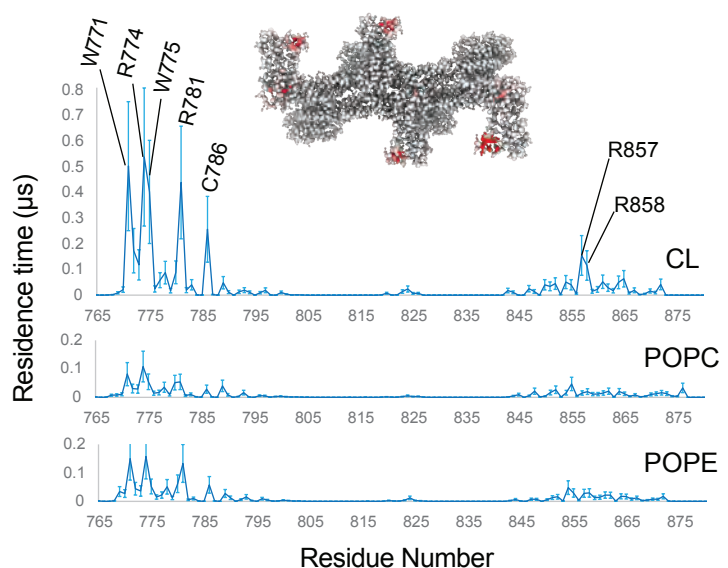
e

MIL
(771-781)

Docking
(857-861)

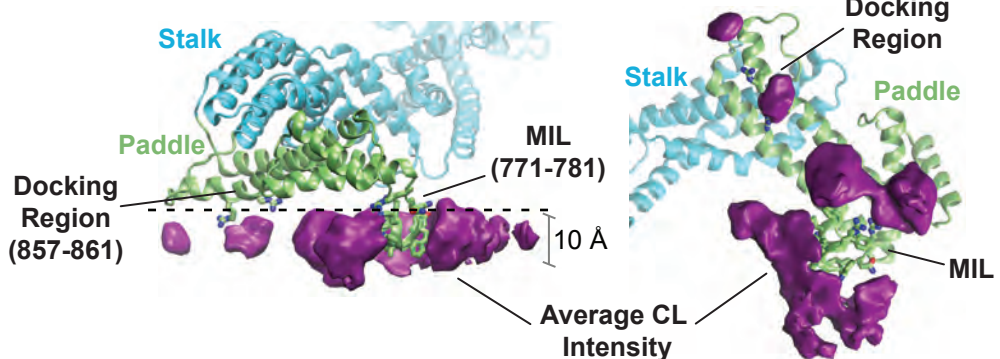


d

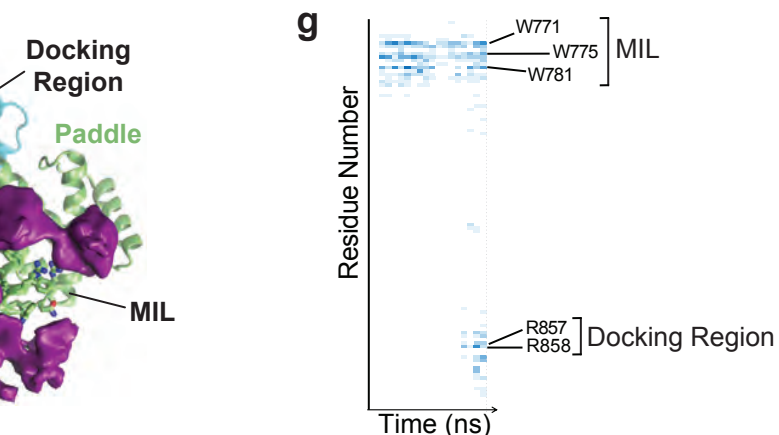


Residue Number

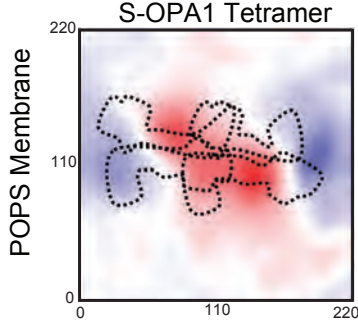
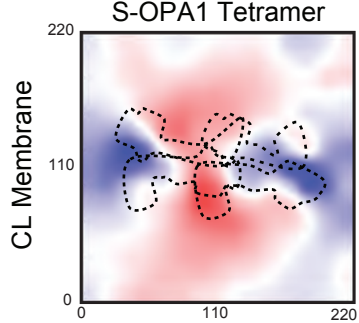
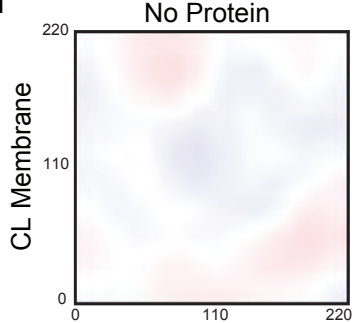
f



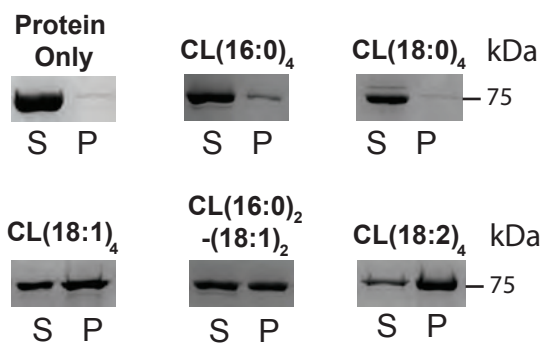
g



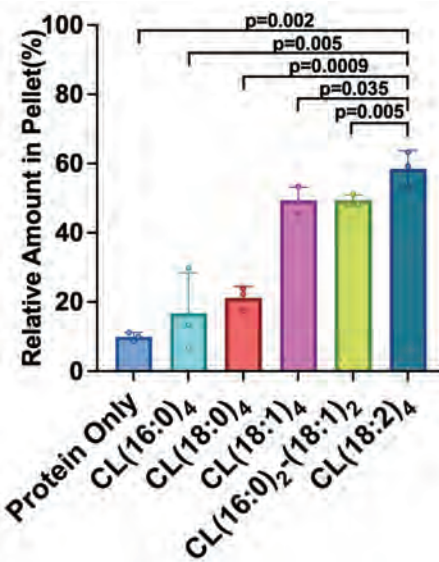
h



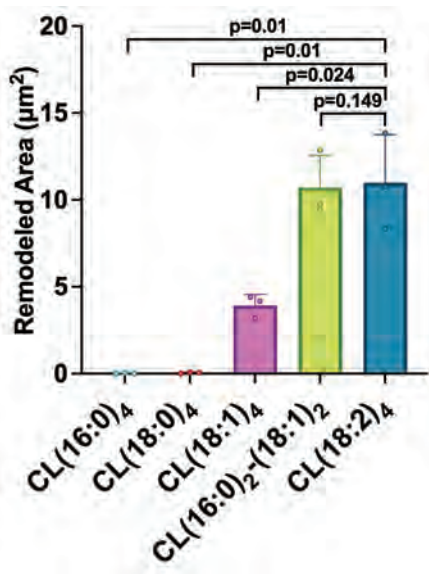
a



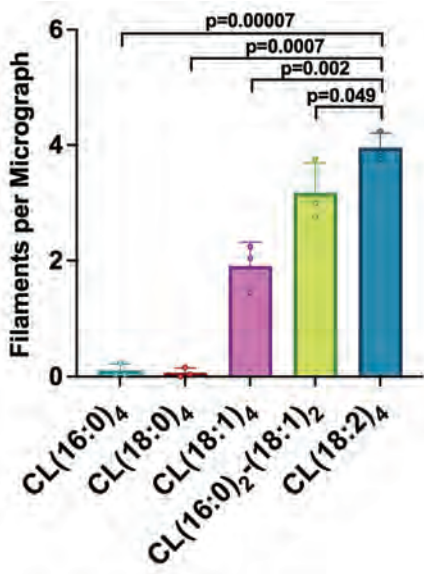
b



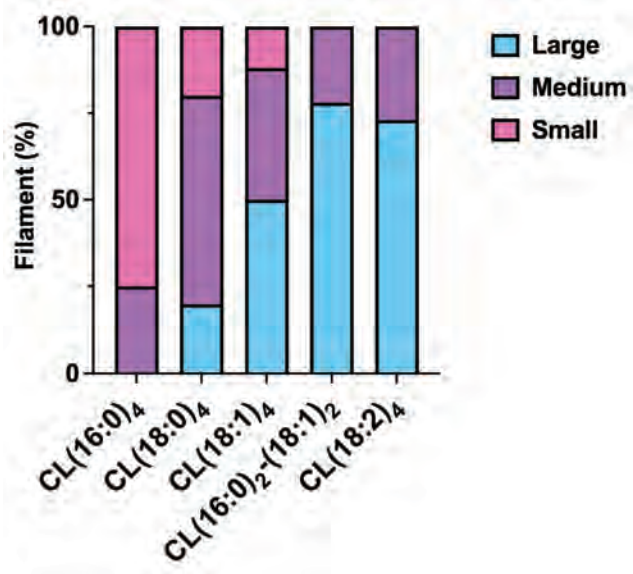
c



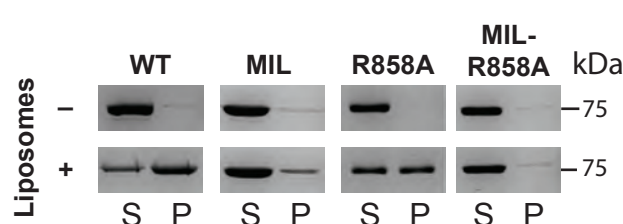
d



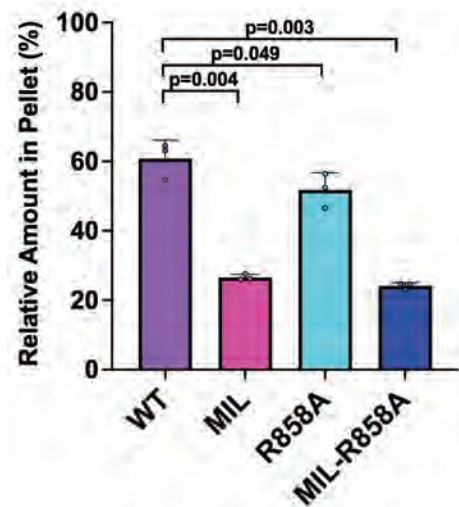
e



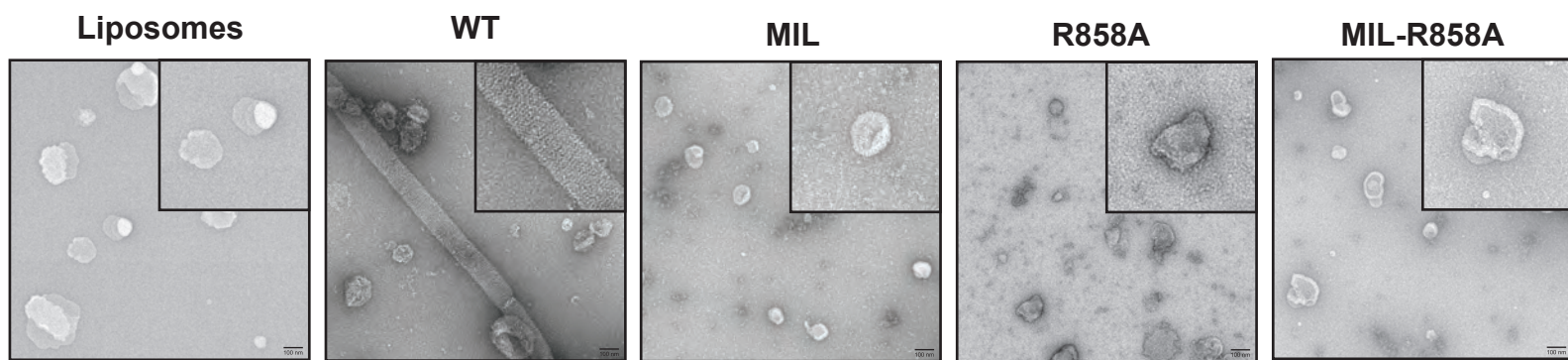
a



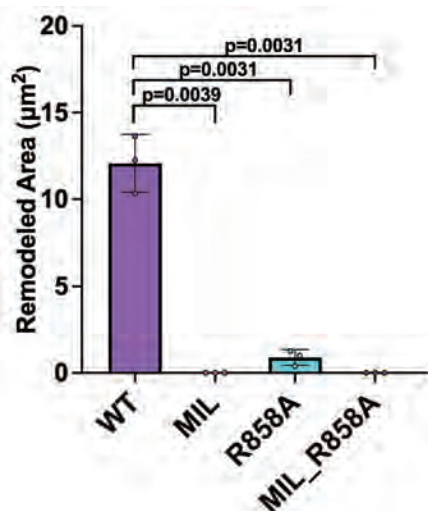
b



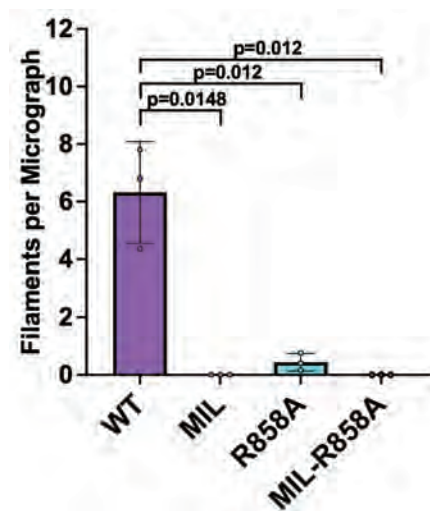
c



d



e



f

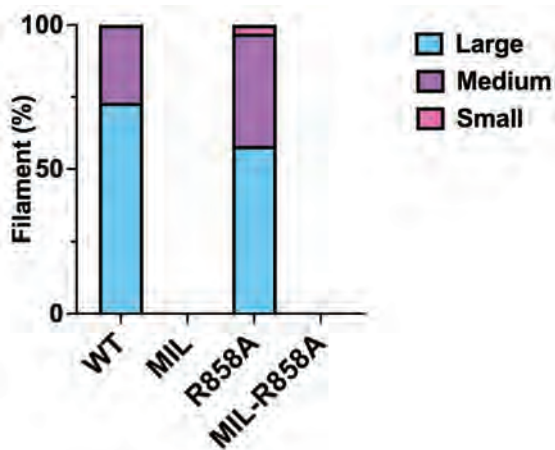


Figure 4

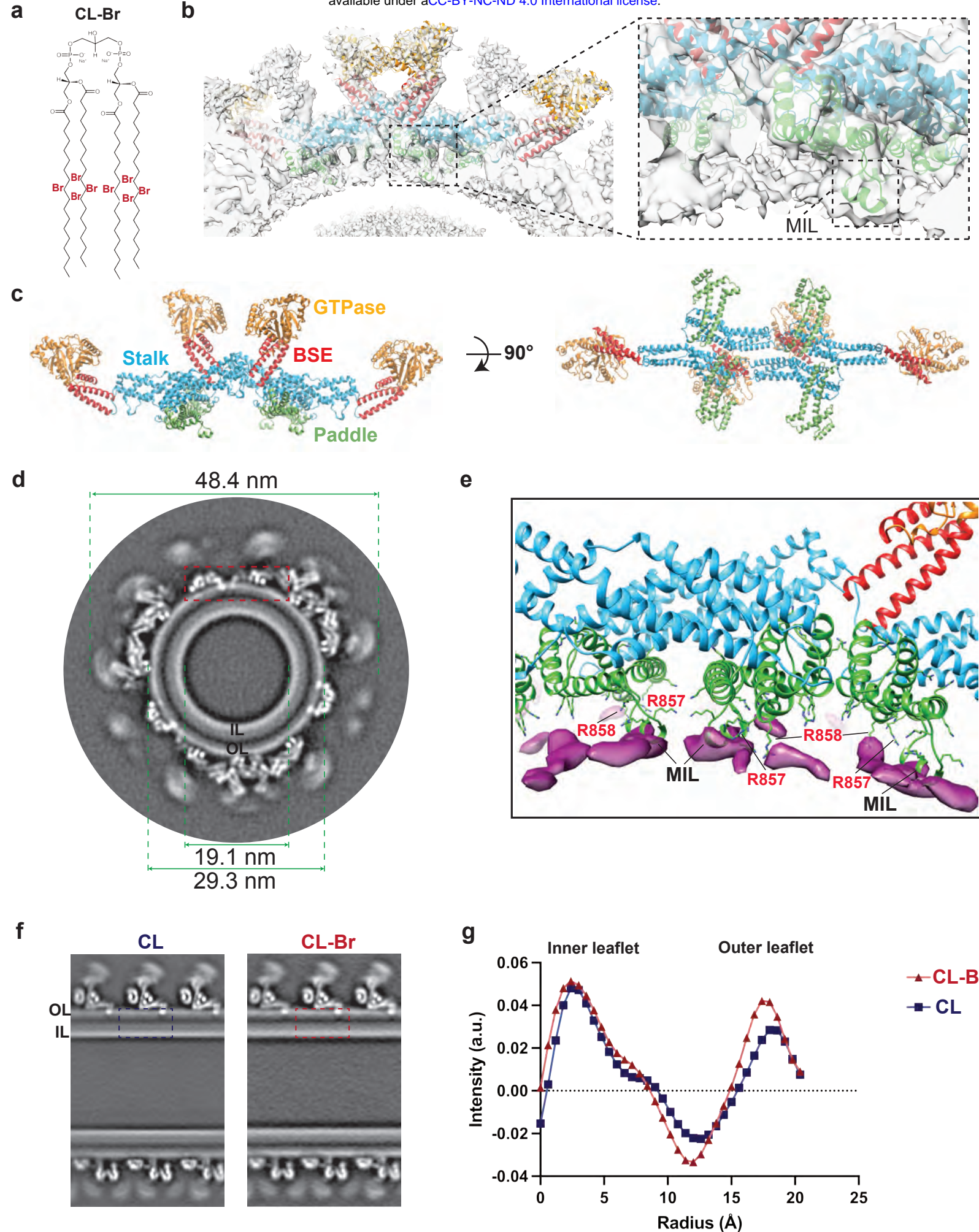
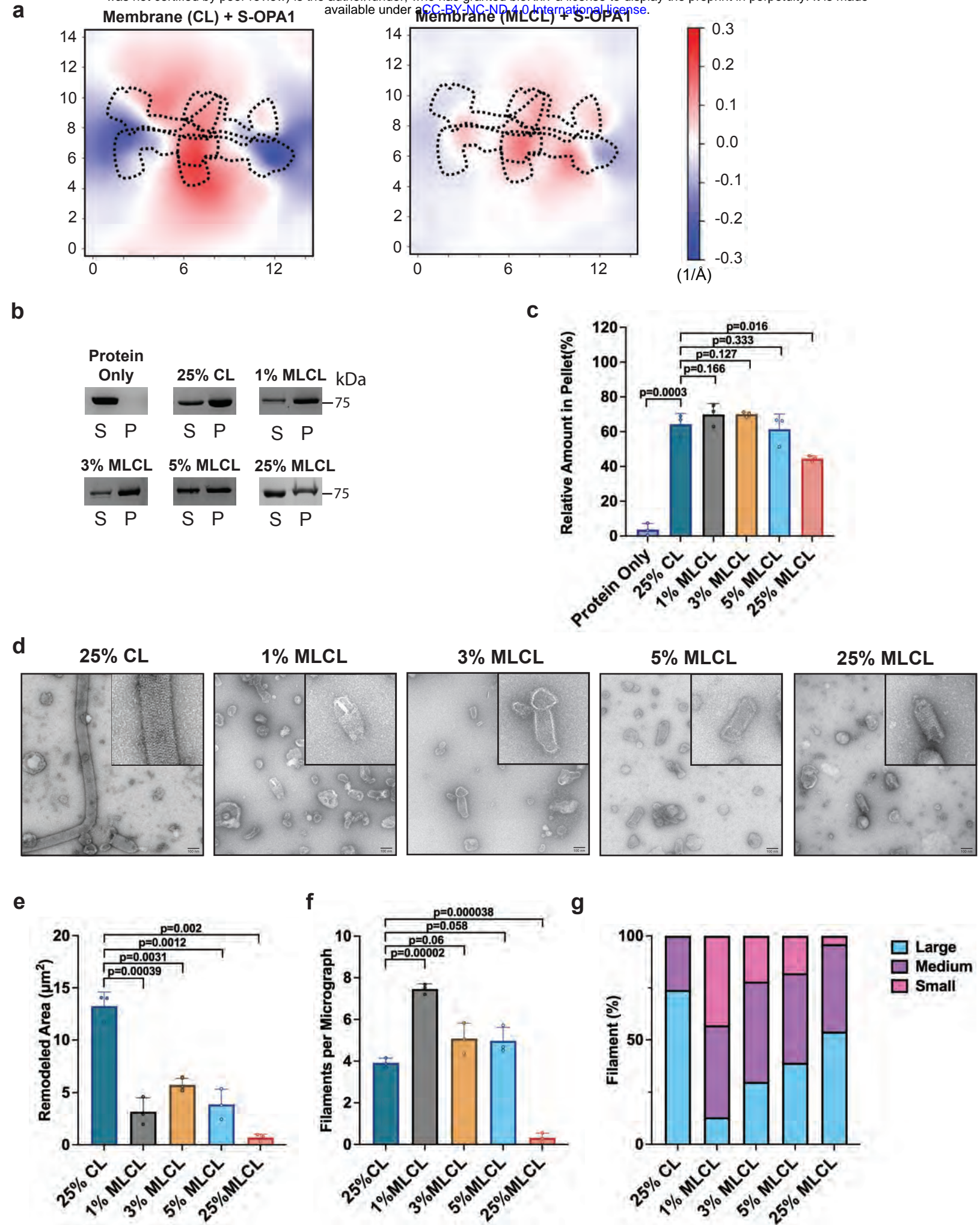
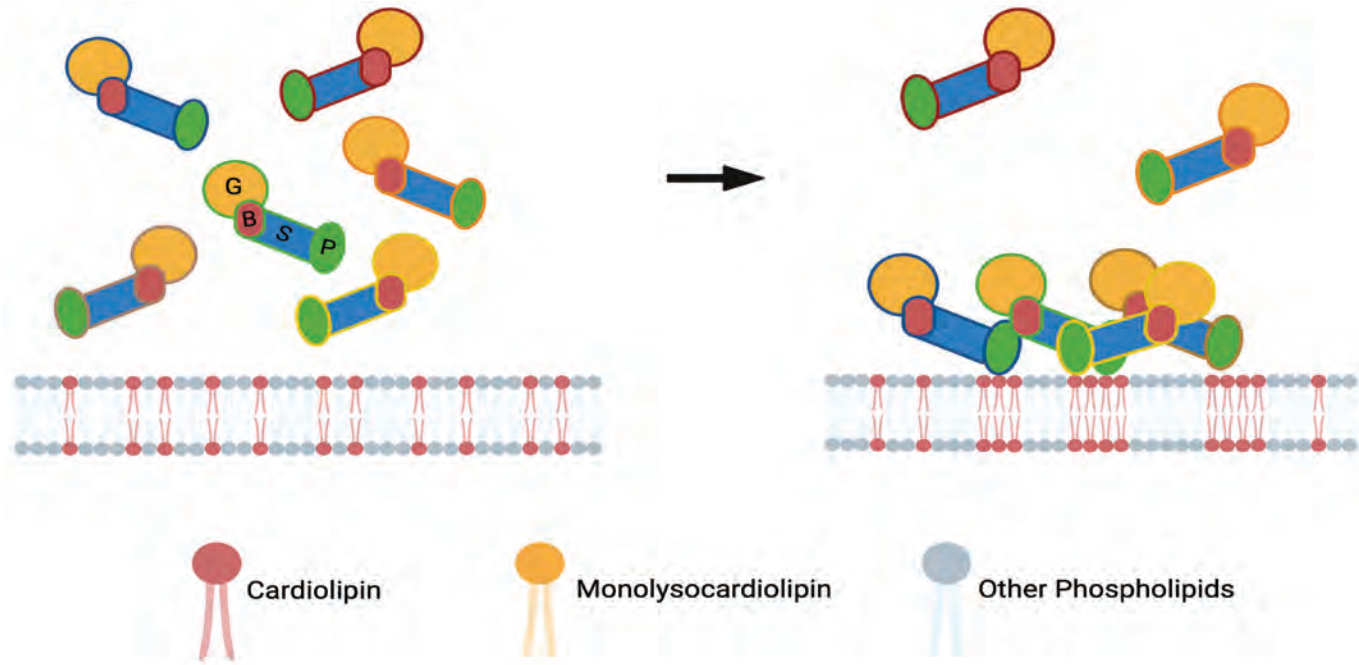


Figure 5



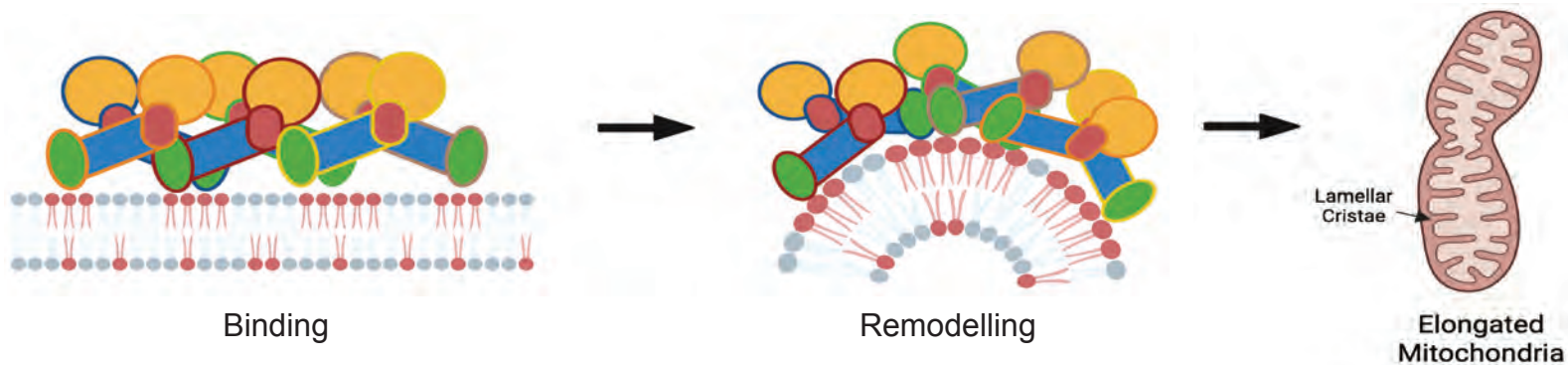
a

OPA1 polymerization on membranes



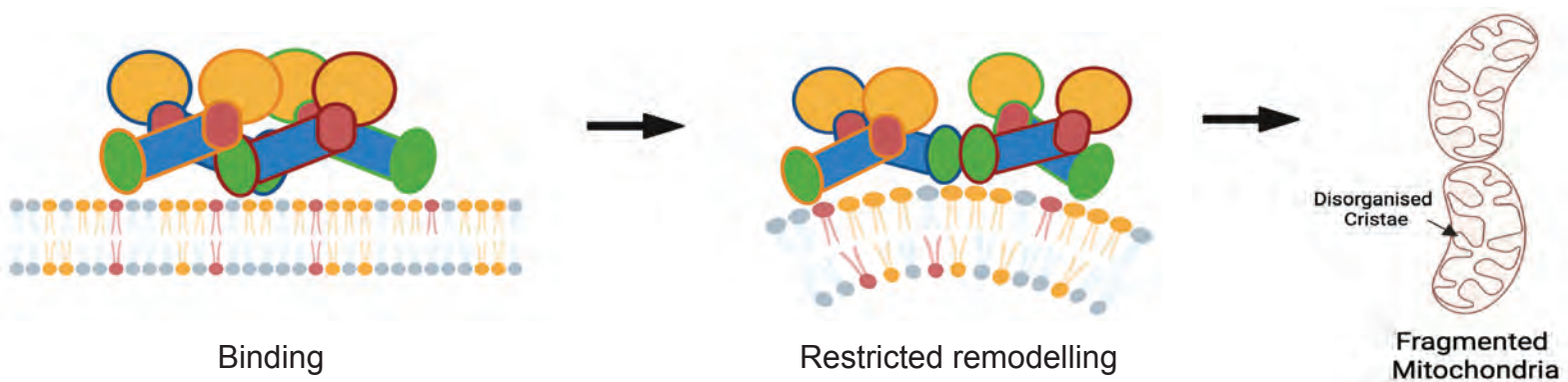
b

CL-enriched membranes



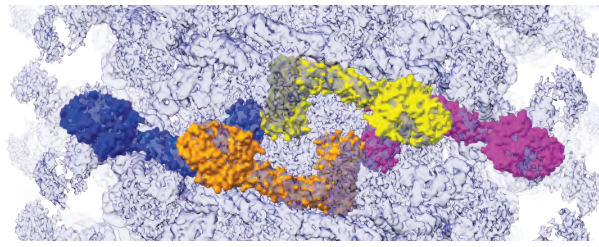
c

MLCL-accumulated membranes



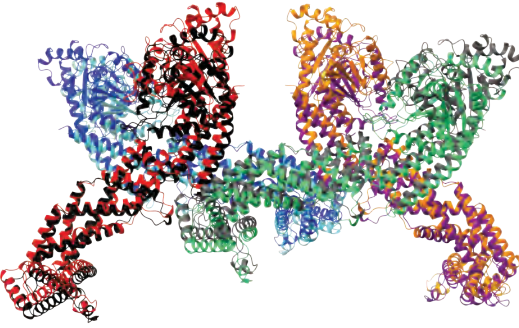
a

Tetramer 2



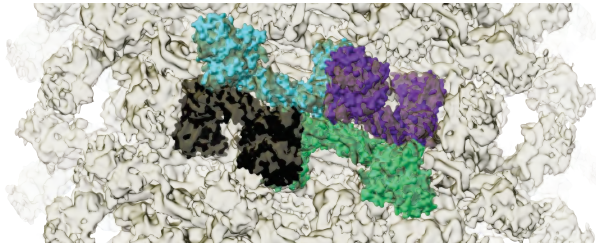
d

RMSD 2.49 Å



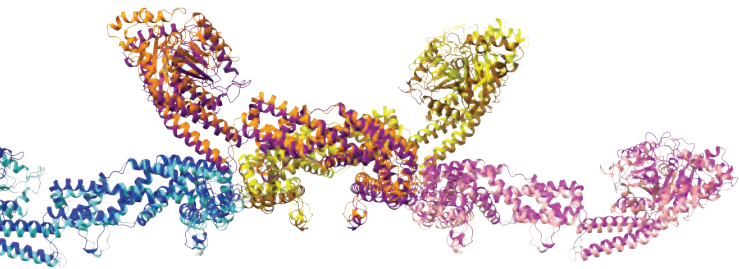
b

Tetramer 3



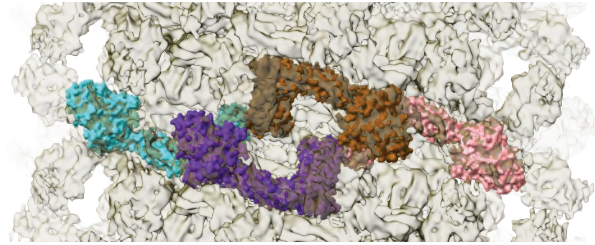
e

RMSD 2.47 Å

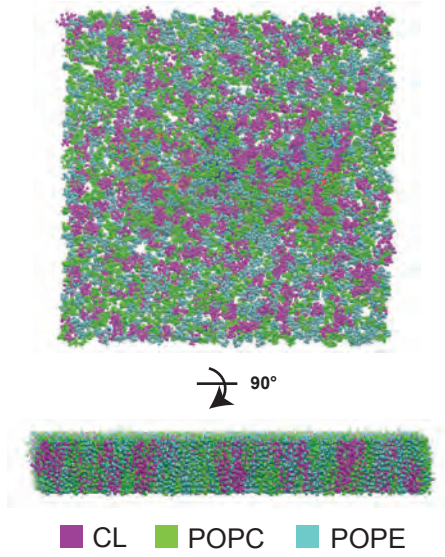


c

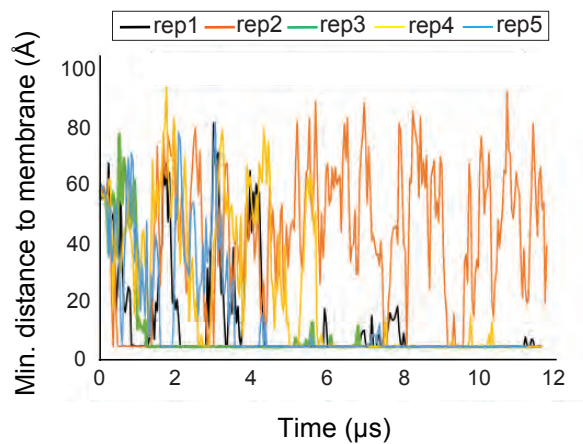
Tetramer 4



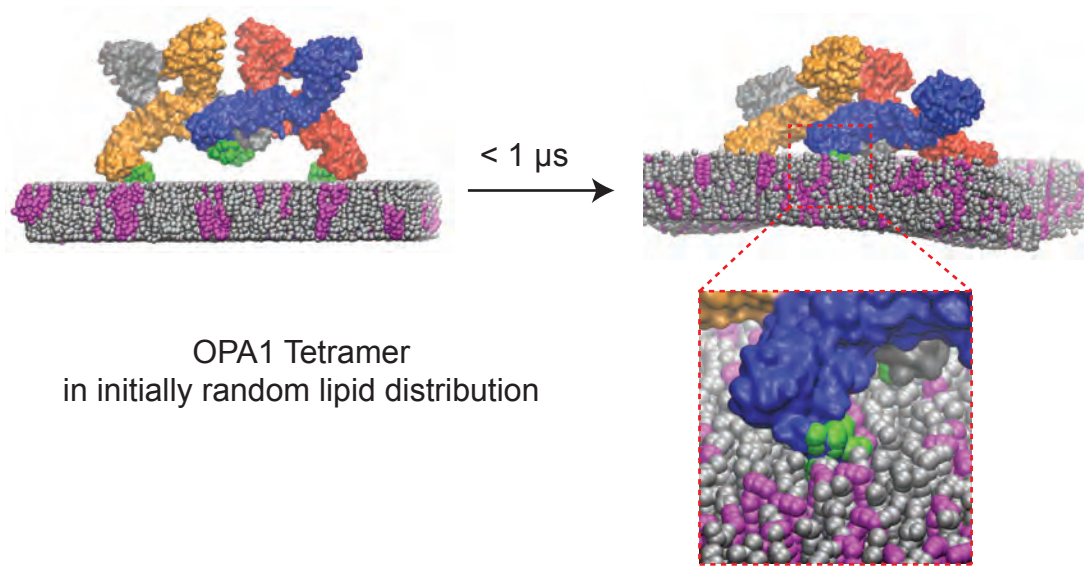
a



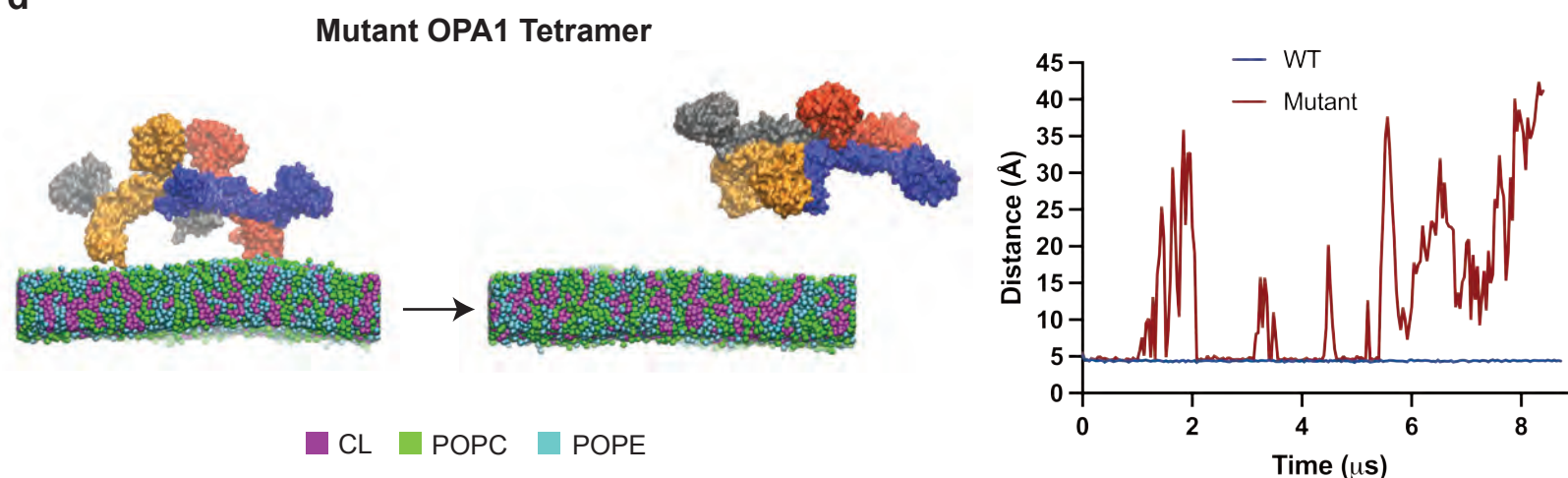
b



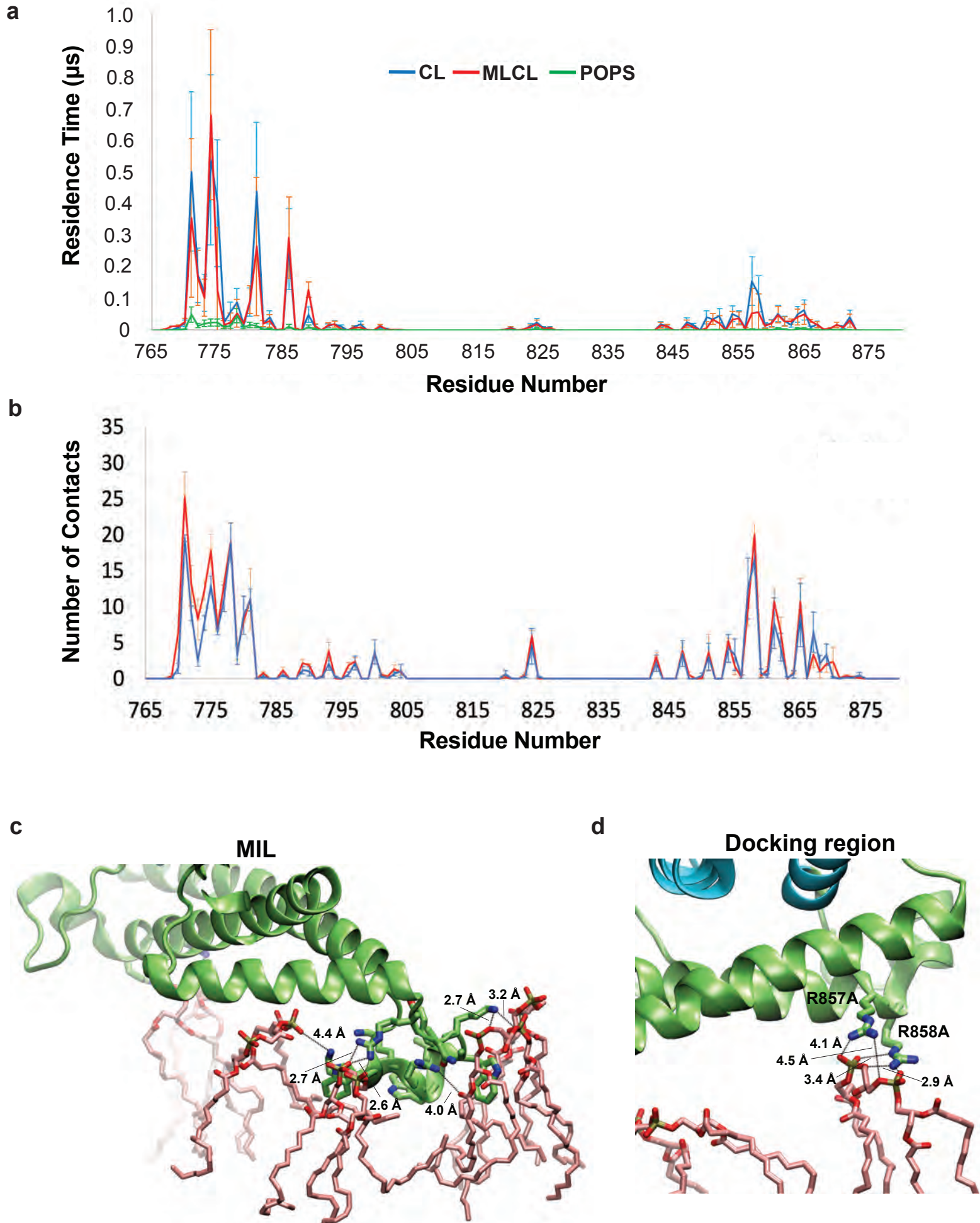
c



d

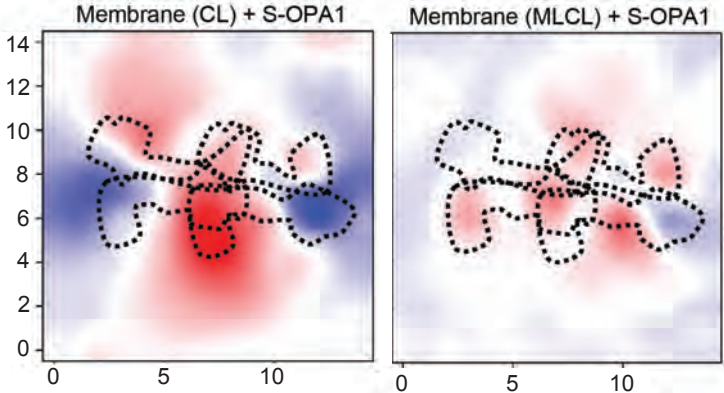


Supplementary Figure 3

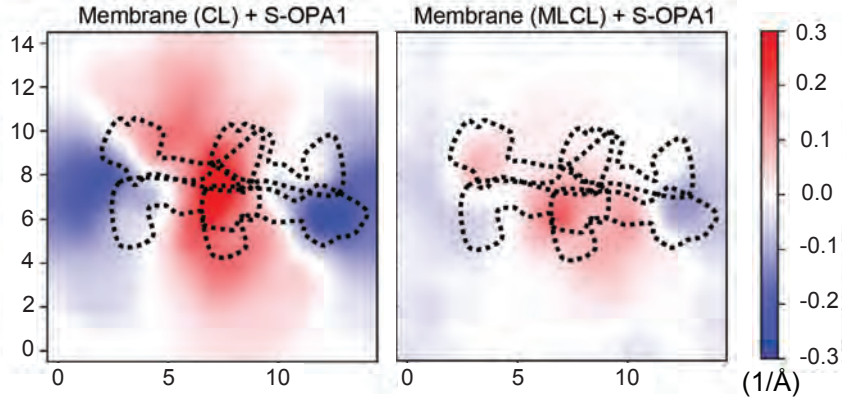


a

Tetramer 1 - Replica 2

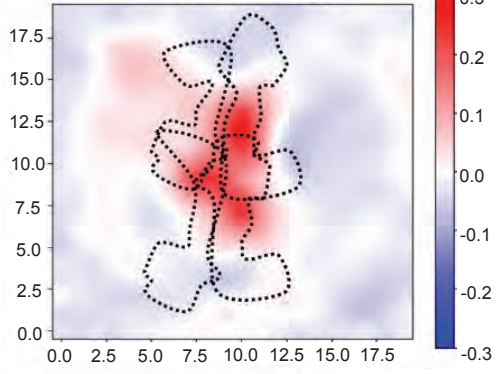


Tetramer 1 - Replica 3

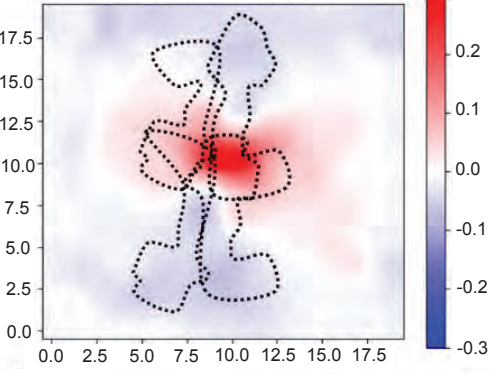


b

Membrane (CL) + S-OPA1

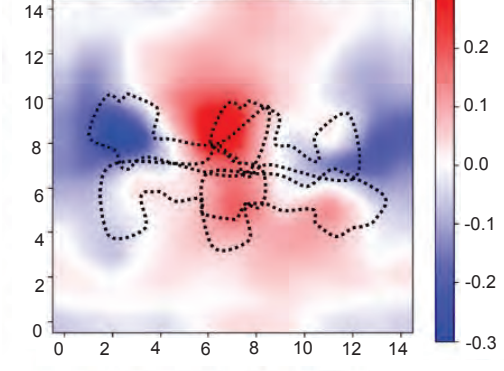


Membrane (MLCL) + S-OPA1

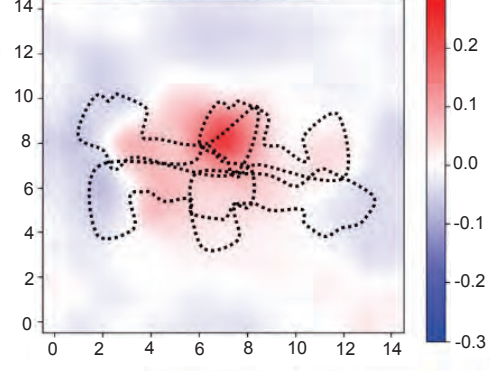


Tetramer 2

Membrane (CL) + S-OPA1

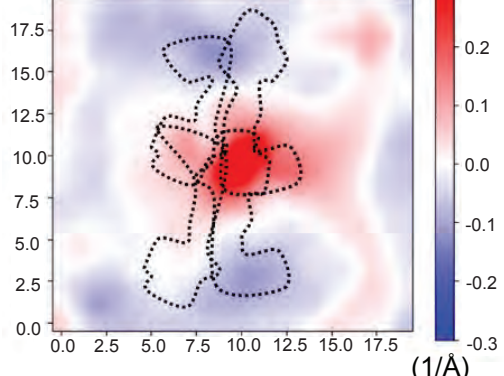


Membrane (MLCL) + S-OPA1

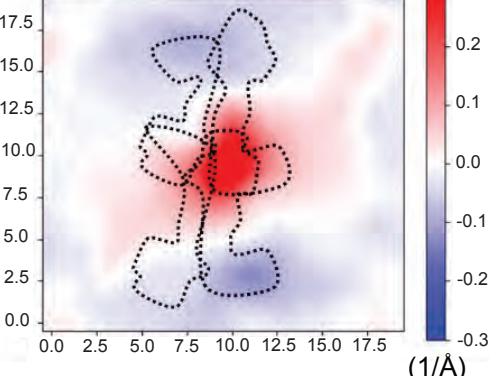


Tetramer 3

Membrane (CL) + S-OPA1



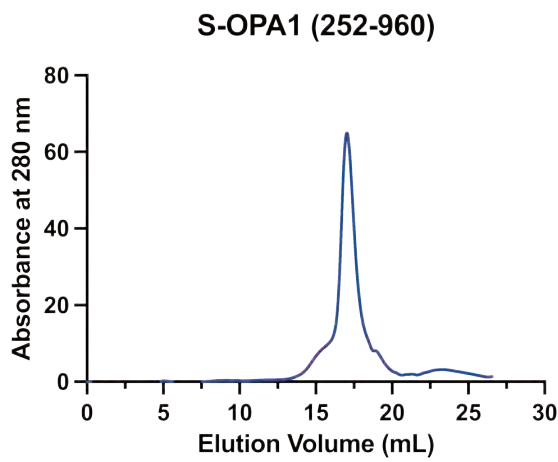
Membrane (MLCL) + S-OPA1



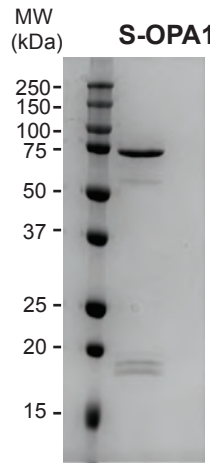
Tetramer 4

Supplementary Figure 5

a



b



c

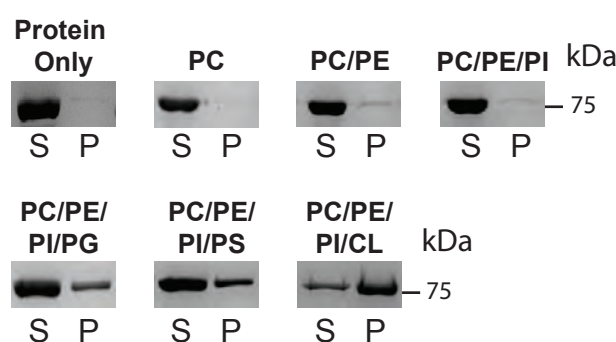
Paddle Domain

sp|O60313|OPA1_HUMAN

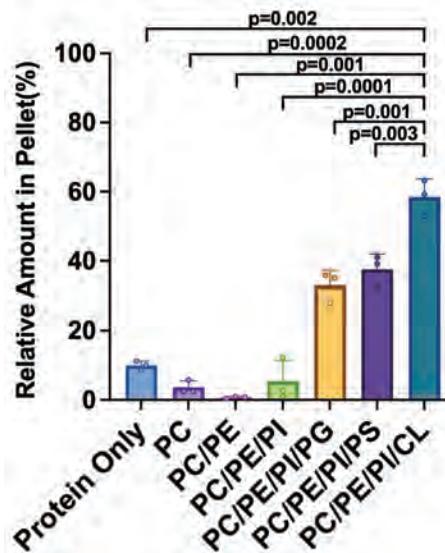
O60313 | Homo sapiens (human)
O39318 | Oncorhynchus mykiss (salmon)
Q5U3A7 | Danio rerio (zebrafish)
A0A4X2MAYE | Vombatus ursinus (wombat)
A0A7N4NVB0 | Sarcophilus harrisii (tasmanian devil)
Q5F499 | Gallus gallus (chicken)
P58281 | Mus musculus (mouse)
Q2TA68 | Ornithorhynchus anatinus (platypus)
F1SF67 | Rattus norvegicus (rat)
F6Z2C8 | Equus caballus (horse)
A0A8C9JPU4 | Panthera tigris altaica (siberian tiger)
A0A337NS50 | Felis catus (cat)
A0A8C9D6G9 | Ursus americanus (black bear)
G1M100 | Allende amboinensis (cat)
A0A813PQW8 | Canis lupus familiaris (dog)
A0A2U4AC4H0 | Tursiops truncatus (dolphin)
A0A2Y9MT19 | Delphinapterus leucas (beluga whale)
A0A452EK44 | Capra hircus (goat)
E1BBC4 | Bos taurus (cow)
H0V6M3 | Cavia porcellus (guinea pig)
G3NG0 | Loxodonta africana (african elephant)
A0A8C5VJK0 | Microcebus murinus (lemur)
F6Y1N1 | Macaca mulatta (rhesus macaque)
A0A815NB02 | Papio anubis (baboon)
Q5RAN3 | Pongo abelii (orangutan)
A0A0D9R952 | Chlorocebus sabaeus (green monkey)
UDY2VY | Callithrix jacchus (marmoset)
A0A2K6P1Z2 | Rhinopithecus roxellana (monkey)
G3S1U3 | Gorilla gorilla (gorilla)
A0A21SSK72 | Pan troglodytes (chimpanzee)
A0A2R9BDG8 | Pan paniscus (bonobo)



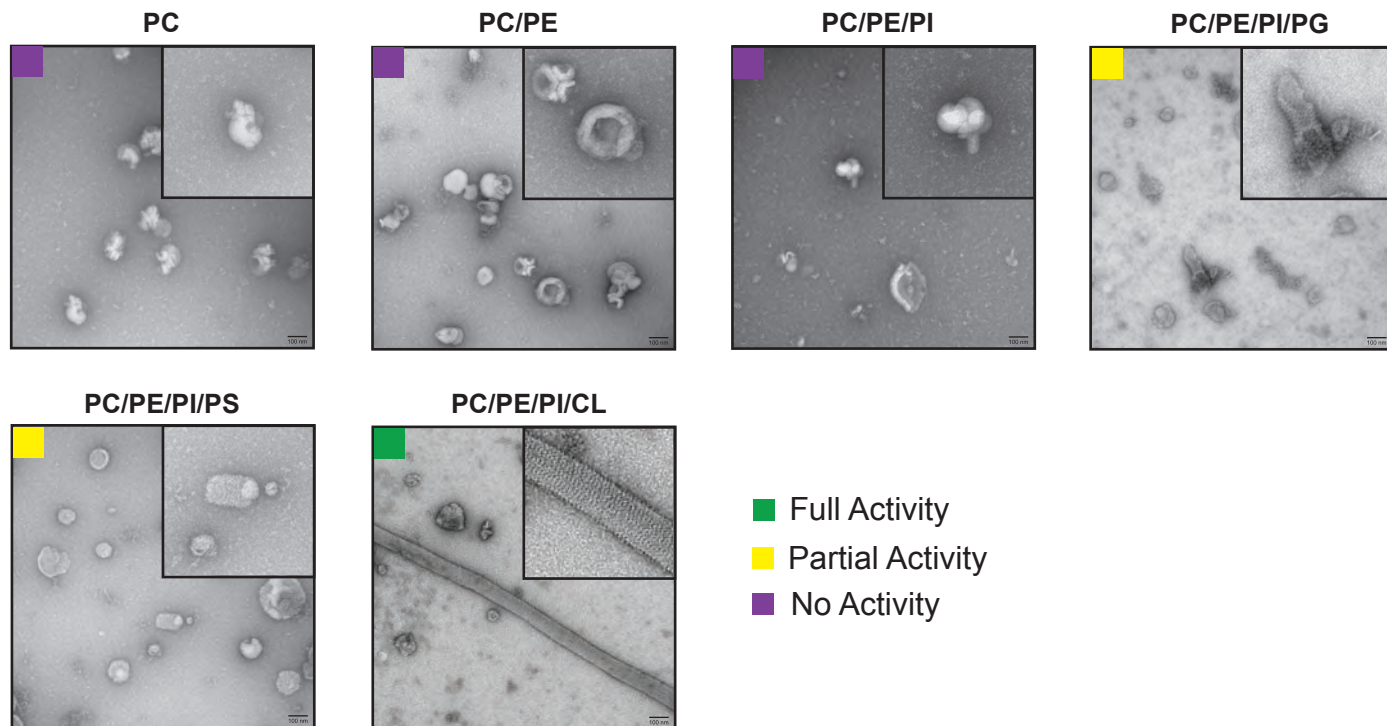
a



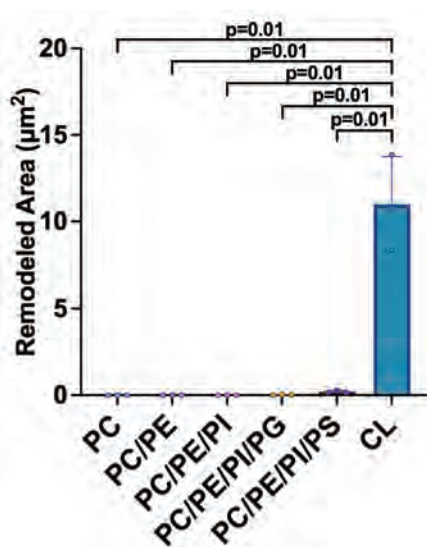
b



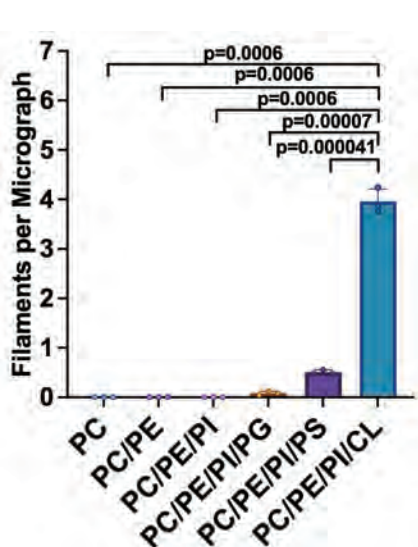
c



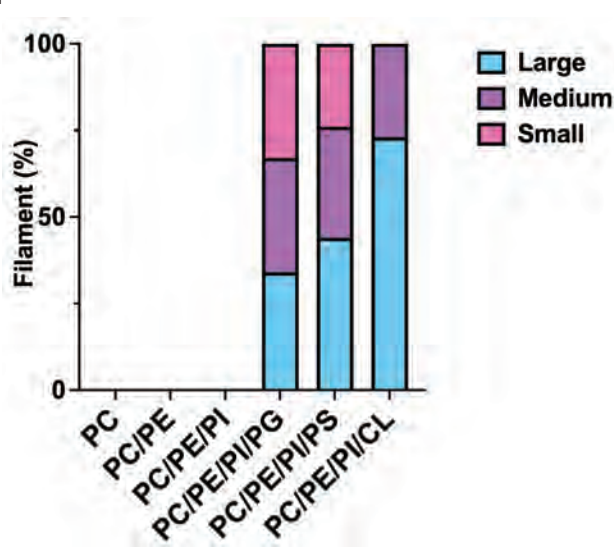
d



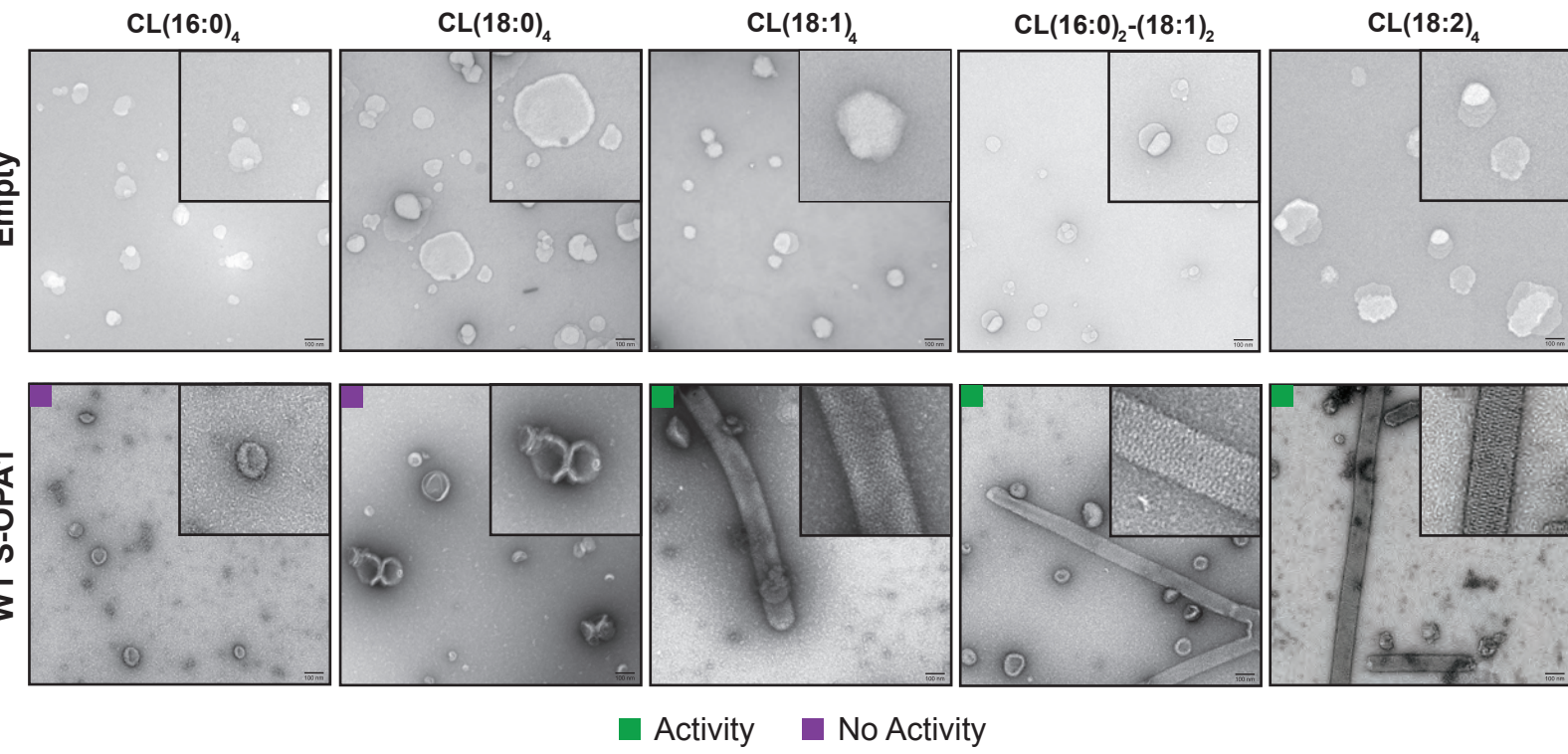
e



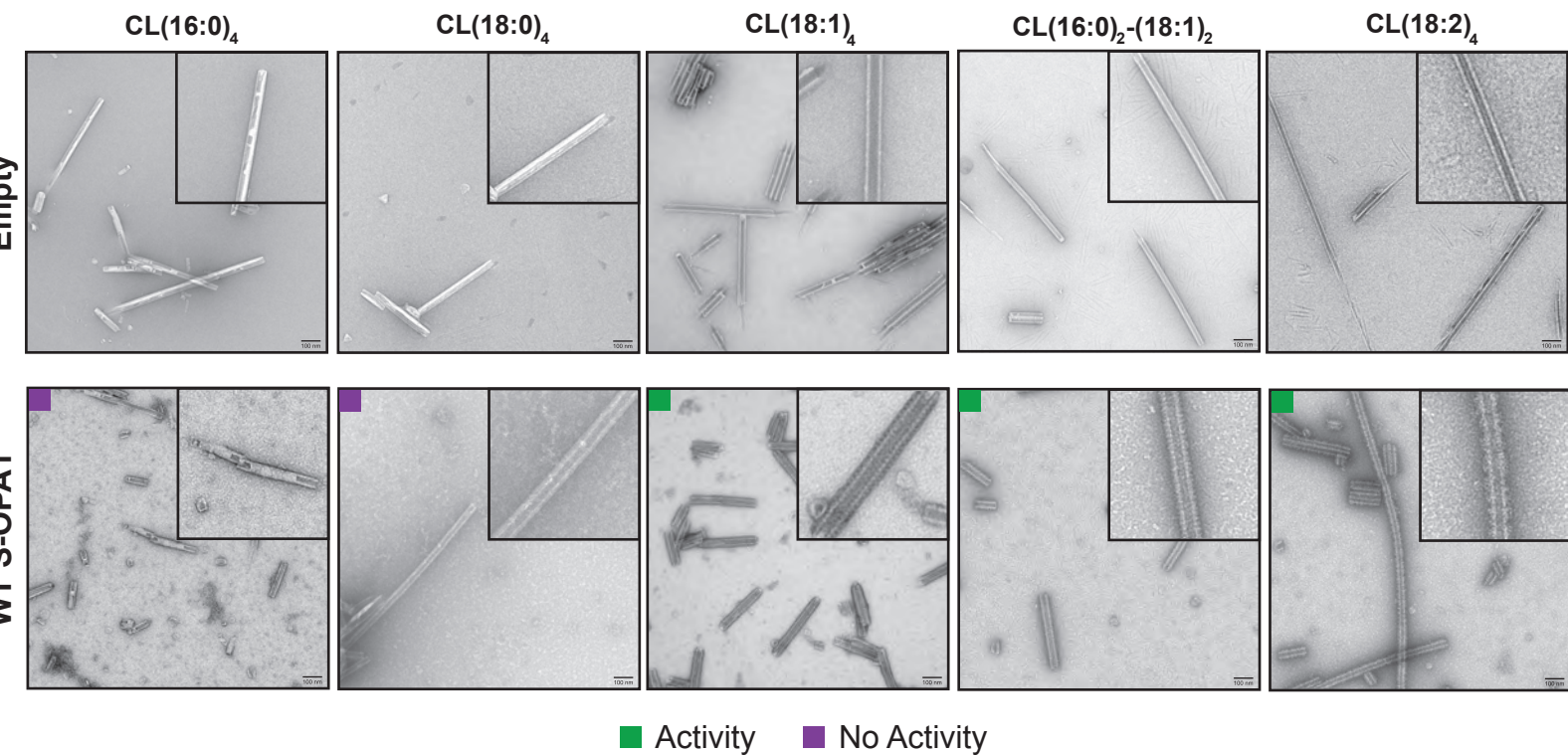
f



a

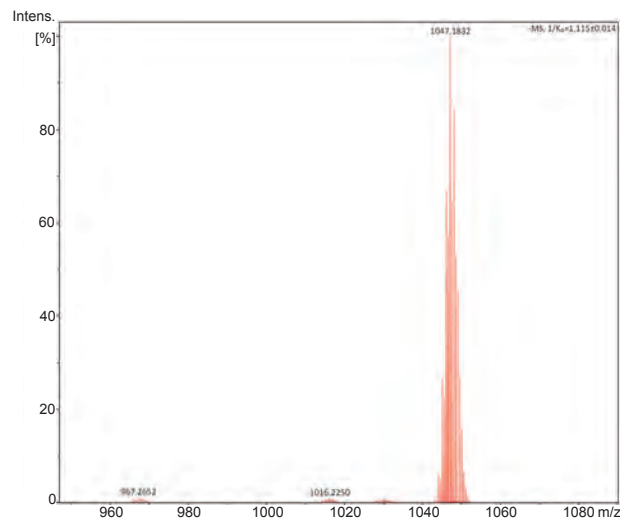


b

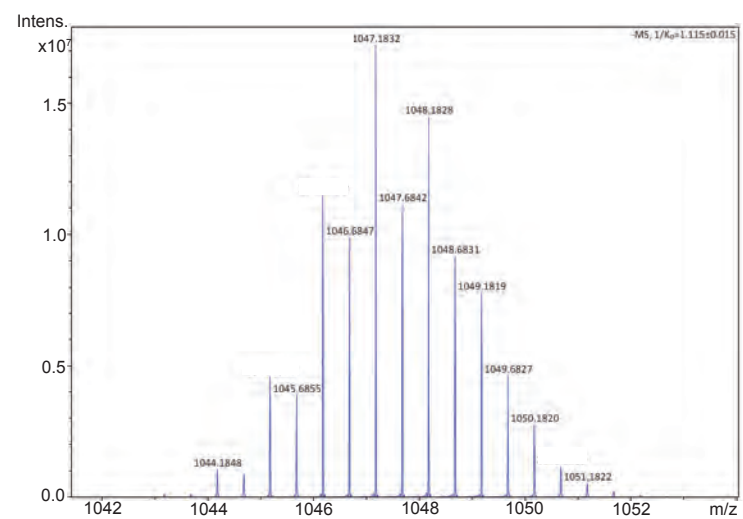


Supplementary Figure 8

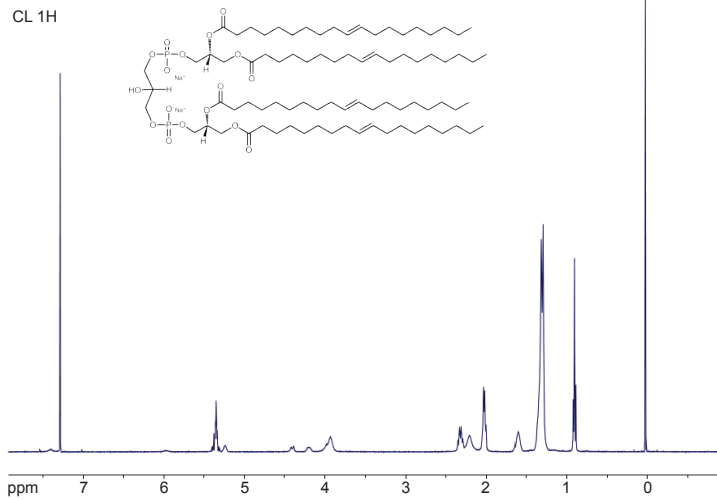
a



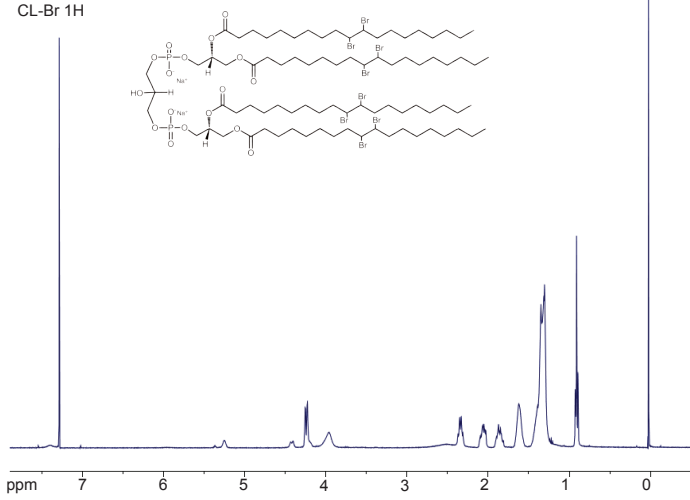
b



c

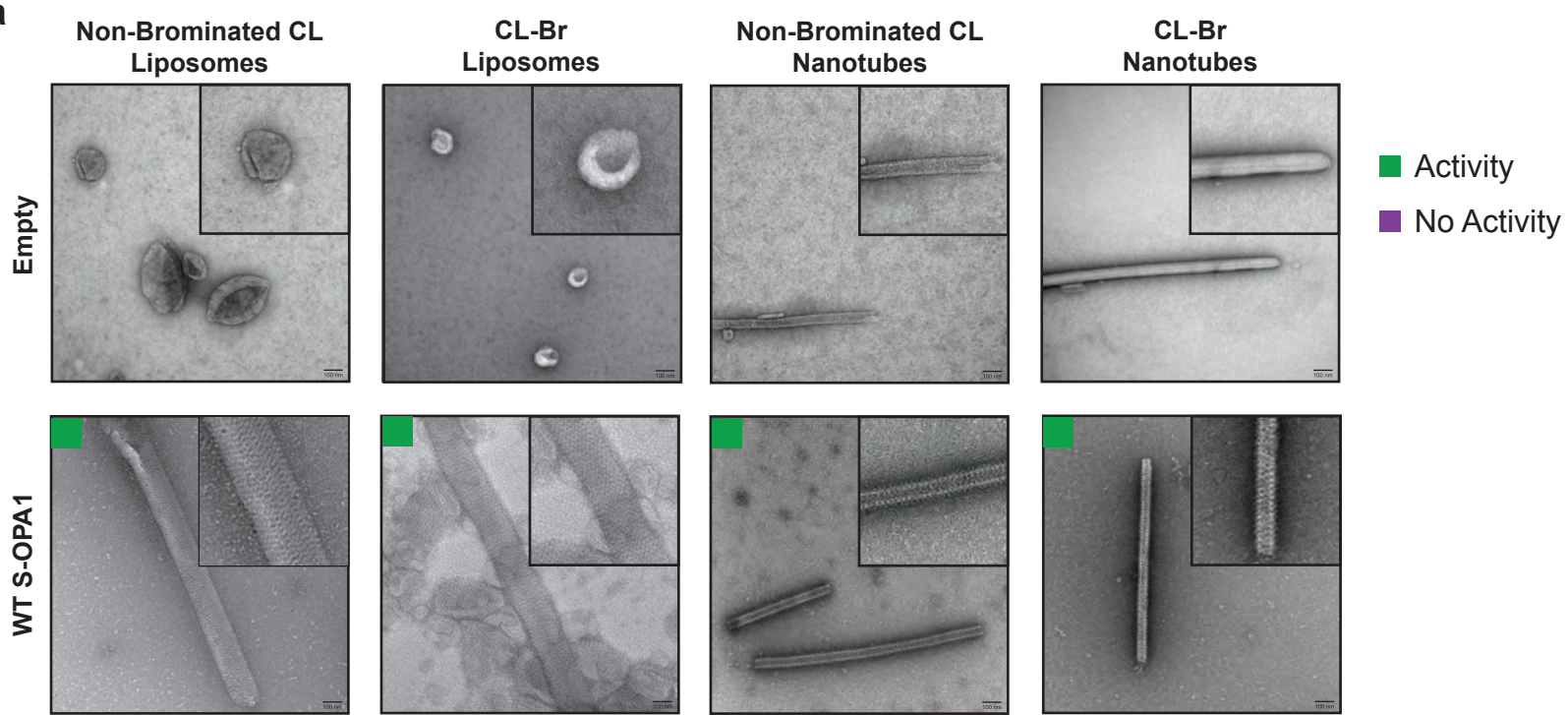


d

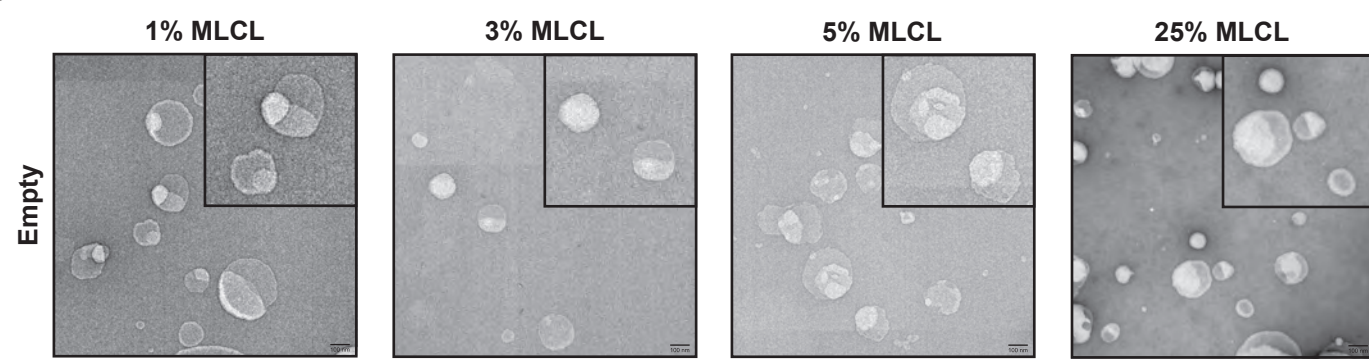


Supplementary Figure 9

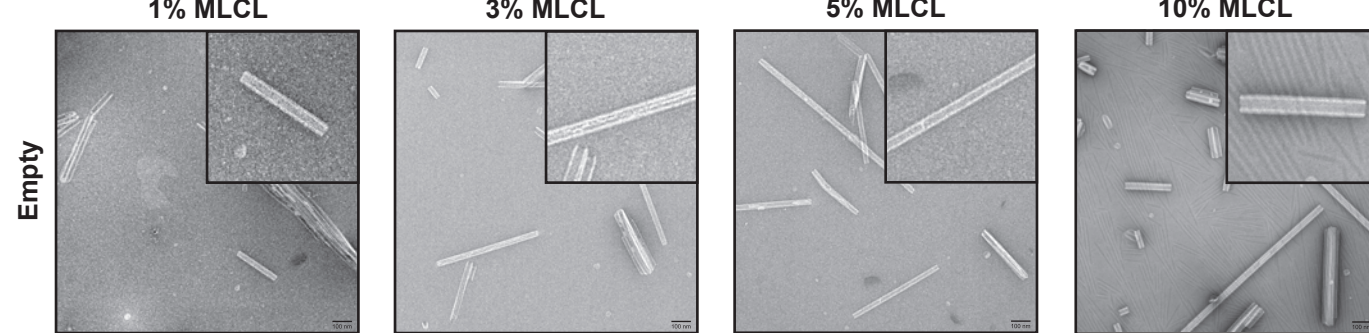
a



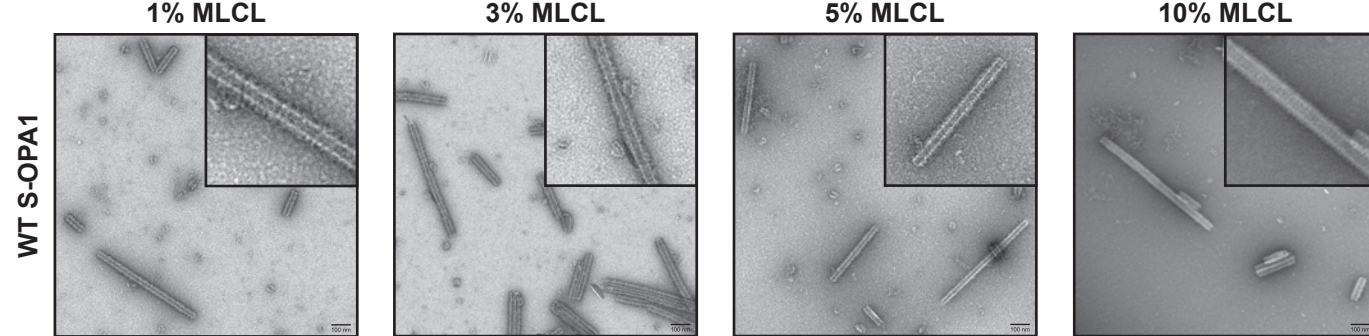
b



c

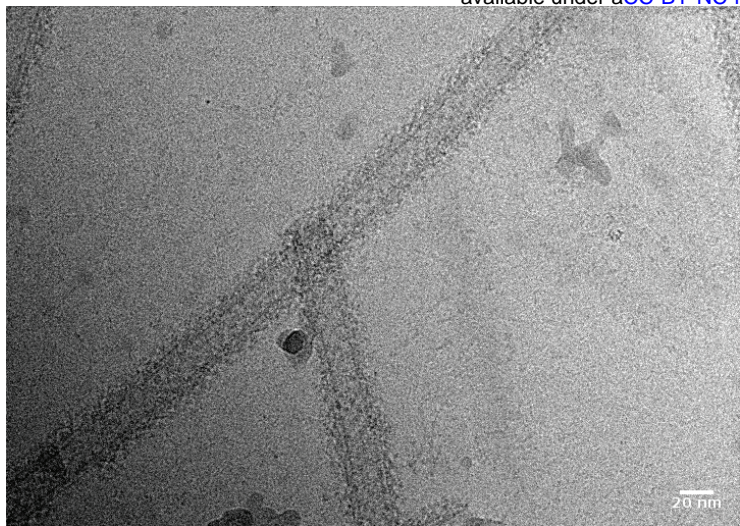


d

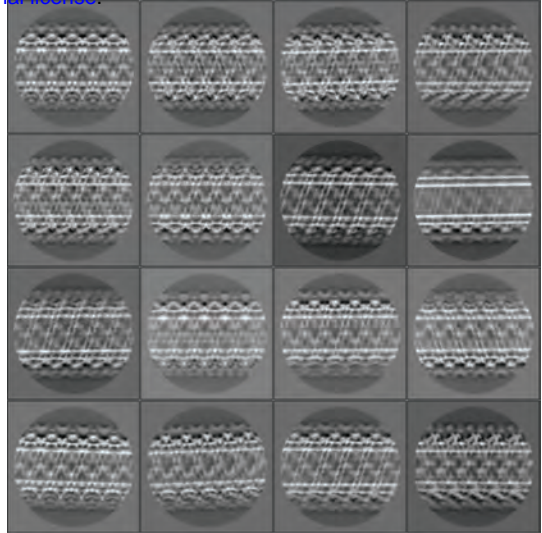


Activity
No Activity

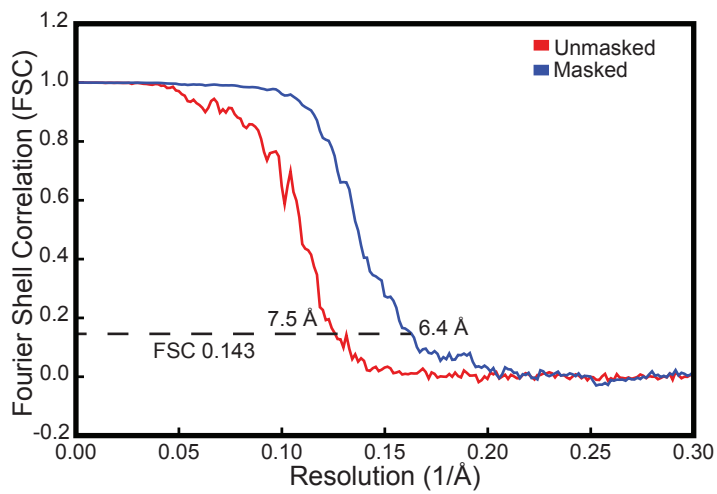
a



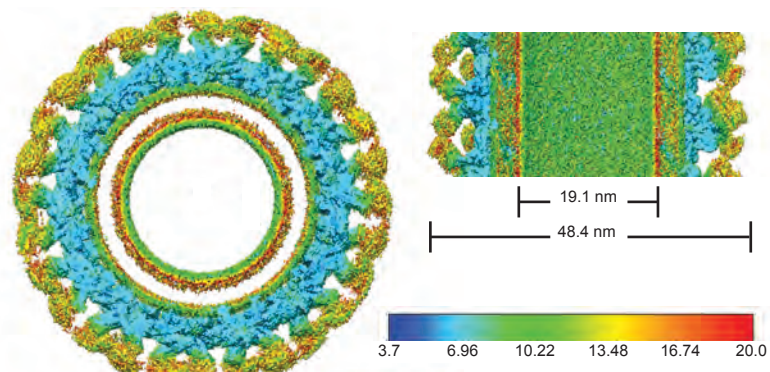
b



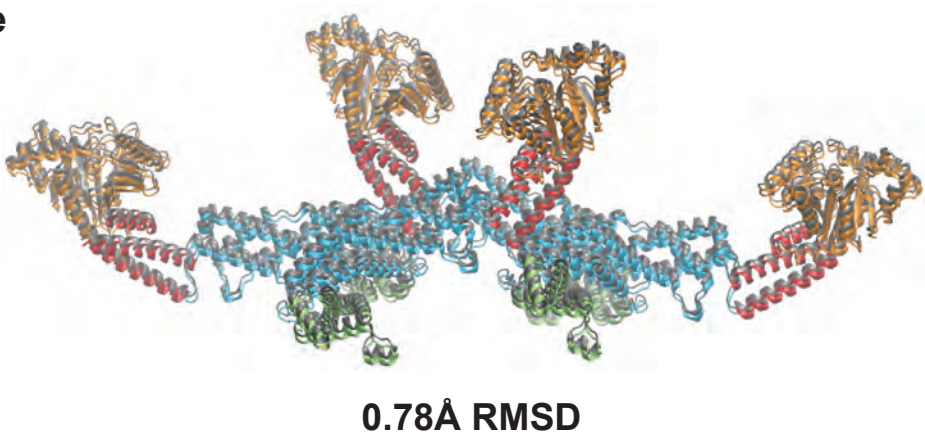
c



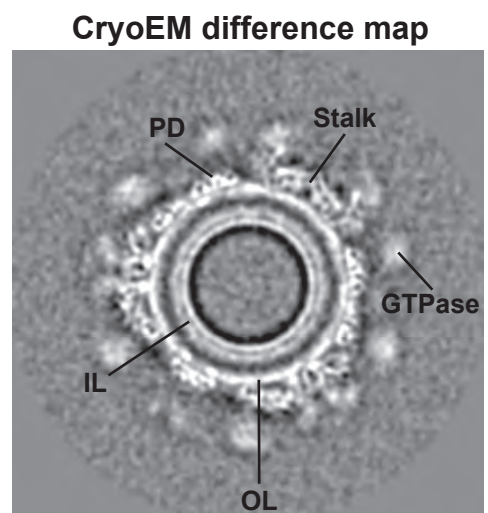
d

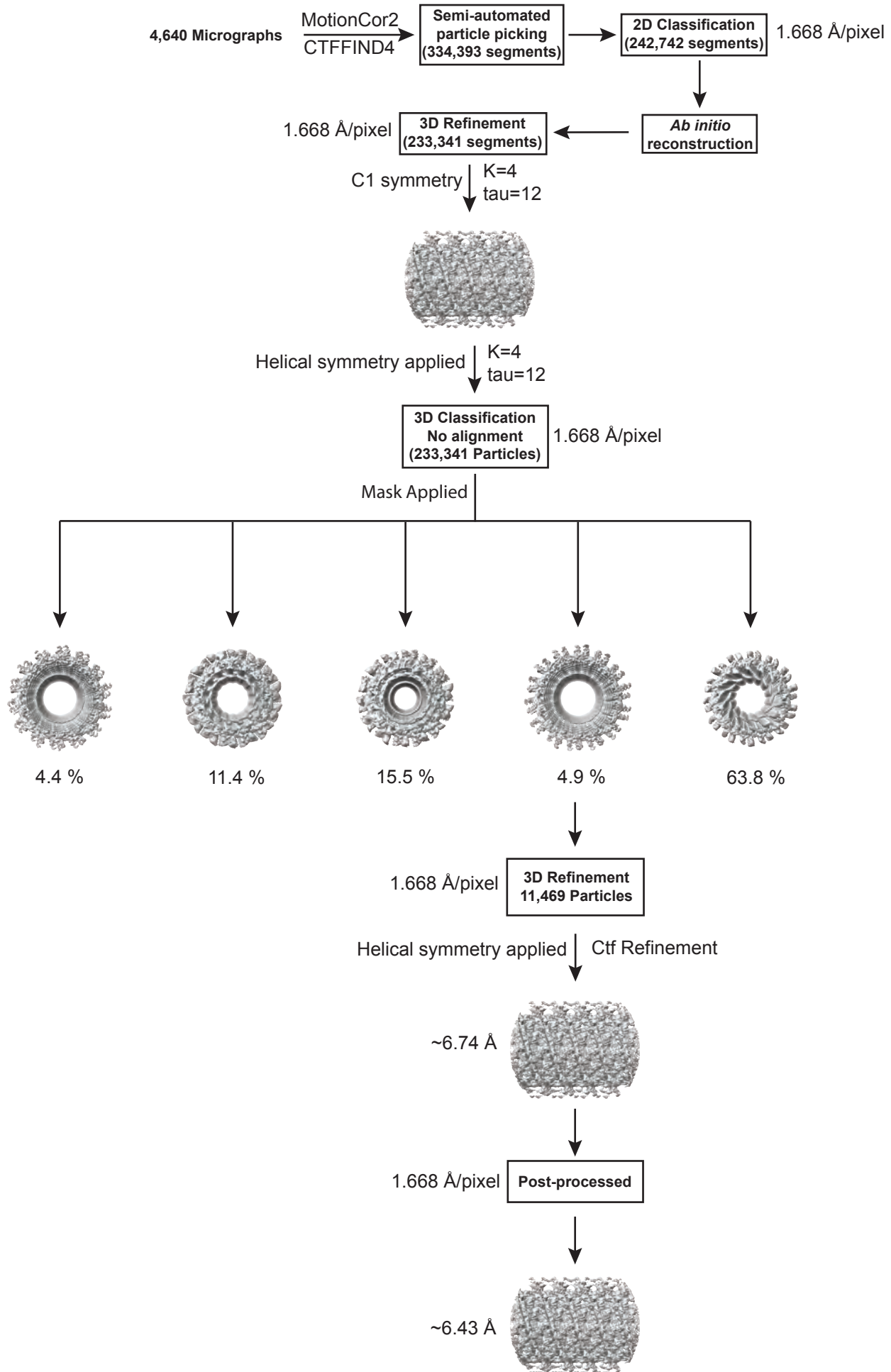


e



f





Human S-OPA1 bound to CL-Br membranes (EMDB-43349)		
Data collection and processing		
Microscope	FEI Titan Krios	
Camera	Gatan K3 Summit	
Magnification	105,000x	
Voltage (kV)	300	
Electron exposure (e ⁻ / Å ²)	65	
Defocus (um)	0.5 to 1.5	
Pixel Size (Å)	0.834	
Symmetry imposed	Helical	
Micrographs (no.)	4,640	
Initial particle images (no.)	233,341	
Final particle images (no.)	11,469	
Map resolution (Å)	6.4	
FSC threshold	0.143	
Map resolution range (Å)	4.8 to 8.1	4.8 to 8.2
Models Generated (PDB code)	8VLZ	8VM4
Refinement		
Initial model used (PDB code)	8CT1	
Model resolution (Å)	6.4	
FSC threshold	0.143	0.143
Map sharpening B factor (Å ²)	-316.754	
Model composition		
Nonhydrogen atoms	22,723	
Protein residues	2,792	
B factors (Å ²) – min		
Protein	112.87	131.06
R.m.s deviations		
Bond lengths (Å)	0.002	0.002
Bond angles (°)	0.385	0.333
Validation		
MolProbity Score	1.16	1.19
Clashscore	3.68	4.06
Poor rotamers (%)	0.0	0.0
Ramachandran plot		
Favored (%)	99.57	99.57
Allowed (%)	0.43	0.43
Disallowed (%)	0.0	0.0

Number	Composition	Components
1	100	POPC
2	78:22	POPC:POPE
3	70:22:8	POPC:POPE:L-PI
4	45:22:8:25	POPC:POPE:L-PI: CL(18:2) ₄
5	45:22:8:25	POPC:POPE:L-PI:POPG
6	45:22:8:25	POPC:POPE:L-PI:POPS
7	45:22:8:24:1	POPC:POPE:L-PI:CL(18:2) ₄ :MLCL(18:2) ₃
8	45:22:8:22:3	POPC:POPE:L-PI:CL(18:2) ₄ :MLCL(18:2) ₃
9	45:22:8:20:5	POPC:POPE:L-PI:CL(18:2) ₄ :MLCL(18:2) ₃
10	45:22:8:25	POPC:POPE:L-PI: MLCL(18:2) ₃
11	45:22:8:25	POPC:POPE:L-PI:CL(16:0) ₄
12	45:22:8:25	POPC:POPE:L-PI:CL(18:0) ₄
13	45:22:8:25	POPC:POPE:L-PI:CL(18:1) ₄
14	45:22:8:25	POPC:POPE:L-PI:CL(16:0) ₂ -(18:1) ₂
15	90:10	Galactosyl(β) Ceramide:CL(18:2) ₄
16	90:9:1	Galactosyl(β) Ceramide: CL(18:2) ₄ :MLCL(18:2) ₃
17	90:7:3	Galactosyl(β) Ceramide: CL(18:2) ₄ :MLCL(18:2) ₃
18	90:5:5	Galactosyl(β) Ceramide:CL(18:2) ₄ :MLCL(18:2) ₃
19	90:10	Galactosyl(β) Ceramide:MLCL(18:2) ₃
20	90:10	Galactosyl(β) Ceramide:CL(16:0) ₄
21	90:10	Galactosyl(β) Ceramide:CL(18:0) ₄
22	90:10	Galactosyl(β) Ceramide:CL(18:1) ₄
23	90:10	Galactosyl(β) Ceramide:CL(16:0) ₂ -(18:1) ₂
24	45:22:8:25	POPC:POPE:L-PI: CL-Br(18:2) ₄
25	90:10	Galactosyl(β) Ceramide:CL-Br(18:2) ₄